Near-infrared variability in dusty white dwarfs: tracing the accretion of planetary material

Laura K. Rogers[1]⋆, Siyi Xu (许偲艺)[2], Amy Bonsor[1], Simon Hodgkin[1],
Kate Y. L. Su[3], Ted von Hippel[1,4], Michael Jura[5]†

[1] *Institute of Astronomy, University of Cambridge, Madingley Road, Cambridge CB3 0HA, UK*
[2] *Gemini Observatory, 670 N. A'ohoku Place, Hilo, HI 96720, USA*
[3] *Steward Observatory, University of Arizona, 933 N Cherry Avenue, Tucson, AZ 85721, USA*
[4] *Department of Physical Sciences, Embry-Riddle Aeronautical University, Daytona Beach, FL 32114, USA*
[5] *Department of Physics and Astronomy, University of California, Los Angeles, CA 90095-1562, USA*

ABSTRACT

The inwards scattering of planetesimals towards white dwarfs is expected to be a stochastic process with variability on human time-scales. The planetesimals tidally disrupt at the Roche radius, producing dusty debris detectable as excess infrared emission. When sufficiently close to the white dwarf, this debris sublimates and accretes on to the white dwarf and pollutes its atmosphere. Studying this infrared emission around polluted white dwarfs can reveal how this planetary material arrives in their atmospheres. We report a near-infrared monitoring campaign of 34 white dwarfs with infrared excesses with the aim to search for variability in the dust emission. Time series photometry of these white dwarfs from the United Kingdom Infrared Telescope (Wide Field Camera) in the *J*, *H* and *K* bands were obtained over baselines of up to three years. We find no statistically significant variation in the dust emission in all three near-infrared bands. Specifically, we can rule out variability at ∼ 1.3% for the 13 white dwarfs brighter than 16th mag in *K* band, and at ∼ 10% for the 32 white dwarfs brighter than 18th mag over time-scales of three years. Although to date two white dwarfs, SDSS J095904.69−020047.6 and WD 1226+110, have shown *K* band variability, in our sample we see no evidence of new *K* band variability at these levels. One interpretation is that the tidal disruption events which lead to large variabilities are rare, occur on short time-scales, and after a few years the white dwarfs return to being stable in the near-infrared.

Key words: white dwarfs – circumstellar matter – infrared: planetary systems – methods: observational – techniques: photometric

1 INTRODUCTION

The atmospheres of polluted white dwarfs have been interpreted as evidence for the survival of outer planetary systems to the white dwarf phase. Observations suggest that between 25–50% of white dwarfs display elements heavier than helium in their atmospheres (Zuckerman et al. 2003, 2010; Koester et al. 2014). The rapid gravitational settling times in comparison to the white dwarfs' cooling age implies ongoing accretion from a reservoir (Koester 2009).

The favoured theory regarding the pollution source is that it originates from planetesimals scattered on eccentric orbits towards the white dwarf where they tidally disrupt, and subsequently accrete on to the atmosphere of the white dwarf. These planetesimals have masses comparable to solar system asteroids (Debes & Sigurdsson 2002; Jura 2003; Farihi et al. 2010a; Jura & Young 2014; Veras et al. 2014). Spectroscopic studies of polluted white dwarfs enable the chemical compositions of the polluting bodies to be determined. These systems uniquely allow the measurement of the bulk compositions of extrasolar planetesimals (e.g. Klein et al. 2011; Jura et al. 2012). To date, 20 different heavy elements have been detected in polluted white dwarfs; in a given star (GD 362) the most heavy elements detected is 19 (e.g. Zuckerman et al. 2007; Xu et al. 2013; Melis & Dufour 2016; Xu et al. 2017). The abundances resemble solar system analogues, with most pollutants resembling bulk Earth

---

⋆ E-mail: laura.rogers@ast.cam.ac.uk
† Deceased

to zeroth order. Some bodies also show evidence for differentiation, posing questions about collisional processing (e.g. Hollands et al. 2018; Harrison et al. 2018).

In addition to atmospheric pollution, G29-38 was the first polluted white dwarf also discovered to show an infrared excess (Zuckerman & Becklin 1987). Follow up observations confirmed its dusty nature (Graham et al. 1990). *Spitzer* drastically increased the number of dust detections around polluted white dwarfs. To date, *Spitzer* has confirmed that nearly 40 white dwarfs display an infrared excess from dust; this is calculated as between 1.5% and 4% of white dwarfs (e.g. Becklin et al. 2005; Kilic et al. 2006; Jura et al. 2007b; Rebassa-Mansergas et al. 2019; Wilson et al. 2019). The temperature of the excess infrared emission is of the order 1000 K (e.g. Jura et al. 2007a), demonstrating the dust lies close to the host star. Eight of the white dwarfs with dust also show evidence of circumstellar gas in emission near the same radius as the dust (Gänsicke et al. 2006, 2007, 2008; Melis et al. 2010; Farihi et al. 2012; Melis et al. 2012; Brinkworth et al. 2012; Debes et al. 2012b).

Additional support for the asteroid tidal disruption model is the discovery of disintegrating planetesimals transiting the polluted and dusty white dwarf WD 1145+017 (Vanderburg et al. 2015). The deepest transit of this star has a period of 4.5 hours and blocks 60% of the flux from the star in the optical (Rappaport et al. 2016; Gary et al. 2017). Another white dwarf, ZTF J013906.17+524536.89, has also been discovered with transit features. The transits cause 30-45% drops in the optical flux, and are separated by 110 days (Vanderbosch et al. 2019).

For the asteroid tidal disruption model, planetary bodies need to be scattered inwards from the surviving outer planetary system of the white dwarf. There are many dynamical mechanisms which can perturb planetesimals on to star-grazing orbits, the favoured theories cite planets as the source. Stellar mass loss can induce instabilities whereby a planet or planets perturb planetesimals on to star-grazing orbits (Debes & Sigurdsson 2002; Bonsor et al. 2011; Veras et al. 2011; Debes et al. 2012a; Mustill et al. 2018). Gänsicke et al. (2019) found evidence for the presence of a close-in planet around a white dwarf, demonstrating planets can survive to the white dwarf phase. Alternative mechanisms to scatter planetesimals include: perturbations due to wide binary companions (Hamers & Portegies Zwart 2016; Veras et al. 2016; Petrovich & Muñoz 2017; Stephan et al. 2017; Smallwood et al. 2018), although Wilson et al. (2019) suggest these may be unimportant, and the liberation of exomoons (Payne et al. 2016).

The scattering of planetary bodies that leads to the pollution is expected to be a stochastic process (Wyatt et al. 2014), with variability predicted on human time-scales. Variations could come in the form of gaseous emission, dusty emission, or total flux caused by transiting debris (as mentioned previously); we may observe variability at optical and infrared wavelengths. These examples have all been seen in polluted white dwarf systems. Variability in the dust emission has been seen for a few white dwarfs. SDSS J095904.69−020047.6 (hereafter WD J0959−0200) and WD 1226+110 demonstrated large drops in dust flux (Xu & Jura 2014; Xu et al. 2018b), whilst WD 0408−041 among other white dwarfs show both increases and decreases in the flux (Farihi et al. 2018; Swan et al. 2019; Wang et al. 2019). Vari-

ability in the strength of the 10 μm dust feature has also be seen for G29-38 (Xu et al. 2018b). Variability in the circumstellar gaseous material has been observed for a handful of white dwarfs (Wilson et al. 2014, 2015; Manser et al. 2015, 2016; Dennihy et al. 2018), this is mostly attributed to the precession of eccentric rings, or planetesimals orbiting within the debris (Manser et al. 2019).

The first white dwarf discovered to show dust emission variability was WD J0959−0200. The 3–5 μm flux dropped by 35% between observations separated by a year and appeared to be stable afterwards, and the near-infrared K band flux dropped by 18.5% between observations separated by 8 years (Xu & Jura 2014). The large K band excess for this white dwarf means the dust is hot and close in. These findings imply the variability event was large and became stable quickly. Motivated by the large variability in WD J0959−0200, we present a study to search for near-infrared variability in 34 white dwarfs with infrared excesses. We aim to characterise how white dwarfs vary in the near-infrared in order to better understand how dusty material arrives in the atmospheres of the white dwarfs.

This paper is structured as follows. Section 2 describes the infrared monitoring campaign over three years for 34 white dwarfs with infrared excesses using the UK Infrared Telescope (UKIRT). Section 3 describes the variability analysis method and the results of this analysis. Section 4 discusses further interpretations from the UKIRT survey and the link with the mid-infrared. Section 5 describes the main conclusions from the study.

2   UKIRT INFRARED MONITORING CAMPAIGN

An infrared monitoring campaign was completed using the Wide Field Camera (WFCAM) on the UKIRT on Maunakea, Hawaii. WFCAM operates in the near-infrared between 0.83 and 2.37 μm; this includes the J, H and K filters (Hewett et al. 2006). WFCAM has four detectors composed of 2048 by 2048 18 micron pixels, with a pixel scale of 0.4″.

Our sample consists of 34 white dwarfs with infrared excesses. Table 1 shows our sample, giving the white dwarf parameters and the nature of the infrared excess. In our sample, 30 white dwarfs have dust emission confirmed with *Spitzer* observations, the 4 remaining objects are identified by WISE and are labelled as dust candidates. *JHK* broadband photometry was obtained for the 34 targets with the UKIRT. 48 hours of UKIRT WFCAM time between semesters 2014B and 2017A were used to study long-term variability in the near-infrared. The dates of the observations for the 34 white dwarfs are shown in Table A1.

Each white dwarf was observed up to 6 times across the 3 year campaign. Our observations probed short time-scales (minutes) between individual frames taken on a given night, and long time-scales (years) between observation dates. Further discussions about time-scales are given in Section 4.3. The observations were designed such that a signal-to-noise ratio (SNR) of 30 was obtained for the J and H bands, and 40 for the K band over the set of observations for that filter. To achieve the required SNR, the brightest white dwarfs in the sample required 25 s of exposure time for the J and H band, and 75 s for the K band. For the faintest white

Table 1. The UKIRT sample of dusty polluted white dwarfs and their properties.

WD Name	Other Name	Gaia DR2 Number	Composition**	T_{eff} [*]	log(g) [*]	Nature of Excess [†]
WD 0010+280	PG 0010+281	2859951106737135488	H	23700	7.73 [1]	Dust [α]
WD 0106−328	HE 0106−3253	5026963661794939520	H	16200	8.03 [1]	Dust [β]
WD 0146+187	GD 16	95297185335797120	He	11500	8.00 [2]	Dust [γ]
WD 0300−013	GD 40	5187830356195791488	He	13600	8.02 [3]	Dust [δ]
WD 0307+077	HS 0307+0746	13611477211053824	H	10100	7.99 [1]	Dust [β]
WD 0408−041	GD 56	3251748915515143296	H	14200	7.96 [1]	Dust [δ]
WD 0435+410	GD 61	203931163247581184	He	15700	8.04 [3]	Dust [ε]
WD J0738+1835*	SDSS J073842.57+183509.6	671450448046315520	He	14000	8.40 [4]	Dust [ζ]
WD J0959−0200*	SDSS J095904.69−020047.6	3829599892897720832	H	13300	8.06 [5]	Dust [η]
WD 1015+161	PG 1015+161	3888723386196630784	H	19200	8.03 [1]	Dust [δ]
WD 1018+410	PG 1018+411	804169064957527552	H	21700	8.05 [1]	Dust [θ]
WD 1041+092	...	3869060540584643328	H	17600	8.12 [1]	Dust [ζ]
WD 1116+026	GD 133	3810933247769901696	H	12600	8.04 [6]	Dust [δ]
WD 1145+017	HE 1145+0145	3796414192429498880	He	15900	8.00 [7]	Dust [ι]
WD 1145+288	...	4019789359821201536	H	12400	7.96 [1]	Cand [κ]
WD 1150−153	EC 11507−1519	3571559292842744960	H	11400	7.98 [1]	Dust [λ]
WD J1221+1245*	SDSS J122150.81+124513.3	3908649148232998400	H	12300	8.20 [5]	Dust [η]
WD 1225−079	PG 1225−079	3583181371265430656	He	10800	8.00 [8]	Dust [β]
WD 1226+110	...	3904415787947492096	H	20900	8.11 [1]	Dust [μ]
WD 1232+563	...	1571584539980588544	He	11800	8.30 [3]	Cand [κ]
WD 1349−230	HE 1349−2305	6287259310145684608	He	18200	8.13 [9]	Dust [ν]
WD 1456+298	G166-58	1281989124439286912	H	7390	8.00 [1]	Dust [ξ]
WD 1504+329	...	1288812212565231232	H	7180	8.06 [10]	Cand [κ]
WD 1536+520	...	1595298501827000960	H	16700	7.70 [6]	Cand [κ]
WD 1551+175	...	1196531988354226560	He	15600	7.96 [11]	Dust [π]
WD 1554+094	KUV 15519+1730	4454599238843776128	H	21800	7.63 [12]	BD+Dust [ρ]
WD J1617+1620*	SDSS J161717.04+162022.4	4465269178854732160	H	13200	8.04 [1]	Dust [ζ]
WD 1729+371	GD 362	1336442472164656000	H	10300	8.13 [6]	Dust [ξ]
WD 1929+011	...	4287654959563143168	H	25400	8.17 [1]	Dust [θ]
WD 2132+096	HS 2132+0941	1742342784582615936	H	13100	7.96 [13]	Dust [π]
WD 2207+121	...	2727904257071365760	He	14800	7.97 [3]	Dust [σ]
WD 2221−165	HE 2221−1630	2595728287804350720	H	9900	8.12 [1]	Dust [β]
WD 2326+049	G29-38	2660358032257156736	H	11200	8.00 [1]	Dust [τ]
WD 2328+107	PG 2328+108	2762605088857836288	H	17900	7.74 [1]	Dust [θ]

Notes:

* No WD name, so an SDSS nickname is used.

** Dominant element in the atmosphere.

[*] The temperature and log(g) come from photometric fits, where possible. For a number of the white dwarfs, if no photometric fit was available, we performed a new fit considering the *Gaia* distances. See Section 4.1 for further information.

[*] Properties of the sample references: (1) This work, (2) Koester et al. (2005), (3) Coutu et al. (2019), (4) Dufour et al. (2012), (5) Farihi et al. (2012), (6) Dufour et al. (2017), (7) Vanderburg et al. (2015), (8) Klein et al. (2011), (9) Voss et al. (2007), (10) Barber et al. (2014), (11) Bergeron et al. (2011), (12) Farihi et al. (2017), (13) Gentile Fusillo et al. (2018).

[†] For the nature of the infrared excess: if the white dwarf has a dust detection confirmed with *Spitzer* observations, it is labelled 'dust' and the reference is that of the *Spitzer* observations, otherwise it is a candidate, and it is labelled 'cand', so the reference highlights the paper at which the dust emission is first referred. WD 1554+094 has a brown dwarf companion and dust.

[†] Nature of infrared excess references: (α) Xu et al. (2015), (β) Farihi et al. (2010b), (γ) Farihi et al. (2009), (δ) Jura et al. (2007b), (ε) Farihi et al. (2011), (ζ) Brinkworth et al. (2012), (η) Farihi et al. (2012), (θ) Rocchetto et al. (2015), (ι) Xu et al. (2018a), (κ) Debes et al. (2011), (λ) Jura et al. (2009a), (μ) Brinkworth et al. (2009), (ν) Girven et al. (2012), (ξ) Farihi et al. (2008), (π) Bergfors et al. (2014), (ρ) Farihi et al. (2017), (σ) Xu & Jura (2012), (τ) Reach et al. (2005).

dwarfs, this required 150 s for the *J* band, 450 s for the *H* band, and 1250 s for the *K* band. As the infrared sky is bright, each frame consisted of a dithered stack of five 5 s or 10 s exposures. Table A2 shows the exposure time for each of the five individual exposures making up the dithered stack. All data obtained with WFCAM were pipeline-processed by the Cambridge Astronomical Survey Unit using standard infrared photometry data reduction steps (CASU, Irwin et al. 2004; Dye et al. 2006).

Further processing using the LIGHTCURVES software[1] was executed to improve the precision of the photometry (Irwin et al. 2007). List driven photometry was performed using a master frame to force the centroid positions for the objects. Here, the master frame is the stacked image of all frames; this increases the SNR of the master frame and reduces errors associated with inaccurately placed centroids. Each frame used in the construction of the lightcurves is

[1] https://github.com/mdwarfgeek/lightcurves

re-aligned to the same set of astrometric calibrators (from 2MASS) as the master frame, which gives significantly improved precision in aperture location when compared to centroiding for faint sources (see Irwin et al. 2007). For a particular object, all frames had an aperture between 3–5 pixels (1.2–2″), depending on which aperture gave the lowest RMS value. Using a large number of non-variable stars, the zero-point shift for each frame was calculated to reduce atmospheric effects, and a 2D polynomial was fitted to the magnitude residuals to minimise the error associated with the position on the detector. LIGHTCURVES outputed a robustly calibrated light curve for each filter and for each object in the catalogue list. For variability searches this is essential as it allows us to probe changes down to the percent level.

3 VARIABILITY ANALYSIS

3.1 Analysis Method

This work aimed to obtain high precision JHK photometry of a sample of dusty white dwarfs and to search for and constrain the level of variability in the photometry over the length of the survey. Throughout the analysis the Vega magnitude system was adopted. In order to robustly study the statistics of the photometry, the same analysis method was applied to all white dwarf observations regardless of the magnitude of the white dwarf and the number of measurements in the J, H and K bands. Gaussians were fitted to the distribution of photometrically corrected magnitudes from the LIGHTCURVES software using all dithered stacked frames, as demonstrated in Fig. 1. The total number of dithered stacked frames for each filter is shown in Table A2, this ranges from 3 to 125, with the median number of frames for the J, H and K bands being 9, 12 and 20 respectively. A Markov Chain Monte Carlo (MCMC) approach was implemented to model the magnitude distribution of each star with a Gaussian profile, yielding posterior distributions for the mean and standard deviation thereof. In our analysis, we adopted the median values from the posteriors. Uniform priors were used for the magnitude between 0 and 20, and standard deviation between 0 and 2. We tested larger upper values for the assumed prior range to test the sensitivity on the parameters. The results remained consistent independent of the size of the prior. A python package, PYMC (Patil et al. 2010), was used for MCMC parameter estimation. Five walkers were used, each resulting in 100,000 posterior samples, with the first 40% of the chain being discarded in the burn-in phase. The Gelman-Rubin statistic (Gelman et al. 1992) was implemented to check for chain convergence. For the two parameters (magnitude and standard deviation), all white dwarfs had values $1.000 < \text{GR} < 1.037$ for the J band, $0.999 < \text{GR} < 1.002$ for the H band, and $1.000 < \text{GR} < 1.005$ for the K band, demonstrating good convergence. The median value of the posterior distribution of the standard deviation was used for the variability measurement. The errors are quoted using the 16th and 84th percentiles of the posterior distribution. This median variability measurement is a robust and reliable way of measuring variability.

To ensure that any variability detected was real, stellar objects in the field of view were analysed using the same approach for comparison. For all field stars the median value of
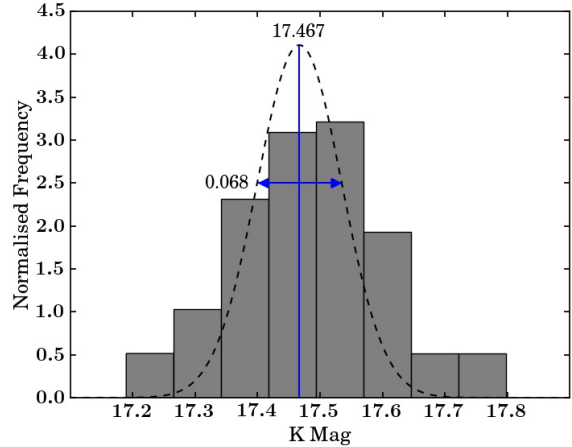
Figure 1. A normalised histogram showing the distribution of photometrically corrected magnitudes from the LIGHTCURVES software using all dithered stacked frames for WD 1145+017. Each dithered stacked frame contains 5×10 second exposures. This white dwarf has 102 measurements in the K band over 782 days. The Gaussian curve shows the median best-fitting Gaussian, with a median magnitude of 17.467, and a median standard deviation of 0.068 mags.

the standard deviation of the Gaussian as a function of magnitude was used to represent the sensitivity of the survey as a function of magnitude. Using the median ensures no variable field stars are contaminating the function. The white dwarfs were then compared to the median MCMC standard deviation of the non-variable field stars at the same magnitude as the white dwarf. If the standard deviation of the white dwarf was significantly higher than that of the field stars, then they were identified as variable. The field objects selected for the comparison were those classified by LIGHTCURVES as stellar and those observed in the same detector as the white dwarf. The number of field stars used in the comparison for each white dwarf ranged from 110 for white dwarfs in sparse fields of view up to 6700 for white dwarfs in densely populated regions. The median number of field stellar objects used in the comparison for each white dwarf was 210.

3.2 Variability Results

Table 2 shows the results of the MCMC runs, and lists the median magnitude and median standard deviation on this magnitude for all white dwarfs in the survey. Fig. 2 plots these median magnitudes and standard deviations for the white dwarfs and field stars in the J, H and K bands. Most white dwarfs have standard deviations which are consistent with that of the field stellar objects. This implies that most of the white dwarfs have J, H and K fluxes which are no more variable than the field stars, which we take to be a proxy of the sensitivity of the survey as a function of magnitude.

A typical spectral energy distribution (SED) for a white dwarf that is representative of our sample peaks in the optical, whereas the dust emission peaks in the infrared. Of the near-infrared bands, the K band is more sensitive to the

Table 2. The resulting median magnitude and standard deviation found from the Gaussian fits to the photometry from the UKIRT observations in the J, H and K bands. The errors are quoted as the 16th and 84th percentiles from the posterior distributions.

WD Name	J Mag	J Std (Mags)	H Mag	H Std (Mags)	K Mag	K Std (Mags)
WD 0010+280	$16.304^{+0.014}_{-0.014}$	$0.016^{+0.019}_{-0.011}$	$16.375^{+0.011}_{-0.010}$	$0.014^{+0.016}_{-0.010}$	$16.345^{+0.019}_{-0.018}$	$0.043^{+0.023}_{-0.019}$
WD 0106−328	$15.616^{+0.009}_{-0.009}$	$0.008^{+0.011}_{-0.006}$	$15.831^{+0.020}_{-0.020}$	$0.041^{+0.026}_{-0.017}$	$15.836^{+0.035}_{-0.034}$	$0.038^{+0.049}_{-0.027}$
WD 0146+187	$15.679^{+0.007}_{-0.007}$	$0.006^{+0.008}_{-0.004}$	$15.650^{+0.010}_{-0.010}$	$0.013^{+0.014}_{-0.009}$	$15.472^{+0.029}_{-0.029}$	$0.060^{+0.039}_{-0.025}$
WD 0300−013	$15.888^{+0.006}_{-0.006}$	$0.006^{+0.007}_{-0.004}$	$15.873^{+0.013}_{-0.013}$	$0.017^{+0.017}_{-0.012}$	$15.861^{+0.014}_{-0.014}$	$0.022^{+0.020}_{-0.015}$
WD 0307+077	$16.274^{+0.013}_{-0.013}$	$0.012^{+0.016}_{-0.008}$	$16.159^{+0.012}_{-0.011}$	$0.016^{+0.017}_{-0.011}$	$16.217^{+0.018}_{-0.018}$	$0.046^{+0.020}_{-0.015}$
WD 0408−041	$16.005^{+0.006}_{-0.006}$	$0.007^{+0.008}_{-0.005}$	$15.909^{+0.012}_{-0.012}$	$0.010^{+0.012}_{-0.007}$	$14.968^{+0.011}_{-0.011}$	$0.012^{+0.014}_{-0.008}$
WD 0435+410	$15.305^{+0.017}_{-0.018}$	$0.022^{+0.055}_{-0.015}$	$15.318^{+0.043}_{-0.037}$	$0.055^{+0.138}_{-0.035}$	$15.271^{+0.011}_{-0.011}$	$0.010^{+0.012}_{-0.007}$
WD J0738+1835	$18.080^{+0.015}_{-0.016}$	$0.026^{+0.022}_{-0.017}$	$17.857^{+0.012}_{-0.012}$	$0.028^{+0.019}_{-0.018}$	$17.329^{+0.011}_{-0.011}$	$0.065^{+0.012}_{-0.012}$
WD J0959−0200	$18.388^{+0.027}_{-0.025}$	$0.044^{+0.037}_{-0.029}$	$18.221^{+0.022}_{-0.021}$	$0.090^{+0.024}_{-0.021}$	$17.809^{+0.015}_{-0.015}$	$0.085^{+0.019}_{-0.019}$
WD 1015+161	$16.044^{+0.013}_{-0.012}$	$0.016^{+0.020}_{-0.011}$	$16.114^{+0.016}_{-0.015}$	$0.019^{+0.023}_{-0.013}$	$16.016^{+0.018}_{-0.018}$	$0.018^{+0.022}_{-0.012}$
WD 1018+410	$16.954^{+0.024}_{-0.022}$	$0.029^{+0.039}_{-0.021}$	$16.964^{+0.025}_{-0.024}$	$0.045^{+0.037}_{-0.024}$	$16.835^{+0.019}_{-0.019}$	$0.026^{+0.026}_{-0.018}$
WD 1041+092	$17.701^{+0.014}_{-0.014}$	$0.014^{+0.016}_{-0.010}$	$17.690^{+0.015}_{-0.015}$	$0.020^{+0.021}_{-0.014}$	$17.761^{+0.018}_{-0.018}$	$0.037^{+0.028}_{-0.024}$
WD 1116+026	$14.852^{+0.008}_{-0.008}$	$0.008^{+0.013}_{-0.006}$	$14.825^{+0.013}_{-0.013}$	$0.013^{+0.023}_{-0.009}$	$14.795^{+0.006}_{-0.007}$	$0.005^{+0.006}_{-0.004}$
WD 1145+017	$17.671^{+0.031}_{-0.031}$	$0.118^{+0.030}_{-0.024}$	$17.680^{+0.015}_{-0.015}$	$0.075^{+0.016}_{-0.014}$	$17.467^{+0.012}_{-0.012}$	$0.068^{+0.015}_{-0.015}$
WD 1145+288	$17.671^{+0.016}_{-0.016}$	$0.015^{+0.017}_{-0.011}$	$17.664^{+0.015}_{-0.015}$	$0.040^{+0.020}_{-0.022}$	$17.281^{+0.012}_{-0.012}$	$0.056^{+0.016}_{-0.017}$
WD 1150−153	$16.236^{+0.007}_{-0.007}$	$0.008^{+0.009}_{-0.006}$	$16.189^{+0.010}_{-0.010}$	$0.011^{+0.012}_{-0.008}$	$15.847^{+0.011}_{-0.011}$	$0.014^{+0.014}_{-0.010}$
WD J1221+1245	$18.413^{+0.029}_{-0.029}$	$0.039^{+0.037}_{-0.027}$	$18.264^{+0.026}_{-0.024}$	$0.103^{+0.029}_{-0.027}$	$17.841^{+0.013}_{-0.013}$	$0.039^{+0.026}_{-0.025}$
WD 1225−079	$14.963^{+0.009}_{-0.008}$	$0.010^{+0.014}_{-0.007}$	$14.960^{+0.015}_{-0.015}$	$0.013^{+0.023}_{-0.010}$	$14.957^{+0.007}_{-0.007}$	$0.012^{+0.010}_{-0.008}$
WD 1226+110	$16.965^{+0.012}_{-0.012}$	$0.011^{+0.013}_{-0.008}$	$16.944^{+0.011}_{-0.011}$	$0.012^{+0.013}_{-0.008}$	$16.623^{+0.015}_{-0.015}$	$0.029^{+0.022}_{-0.019}$
WD J1234+5606	$18.279^{+0.023}_{-0.023}$	$0.035^{+0.032}_{-0.023}$	$18.240^{+0.023}_{-0.022}$	$0.056^{+0.032}_{-0.033}$	$17.797^{+0.021}_{-0.020}$	$0.122^{+0.022}_{-0.020}$
WD 1349−230	$17.018^{+0.011}_{-0.011}$	$0.016^{+0.015}_{-0.011}$	$17.056^{+0.013}_{-0.013}$	$0.022^{+0.019}_{-0.015}$	$16.982^{+0.018}_{-0.017}$	$0.031^{+0.027}_{-0.021}$
WD 1456+298	$14.995^{+0.013}_{-0.012}$	$0.020^{+0.025}_{-0.012}$	$15.062^{+0.012}_{-0.012}$	$0.012^{+0.021}_{-0.009}$	$14.830^{+0.009}_{-0.009}$	$0.014^{+0.013}_{-0.010}$
WD 1504+329	$18.234^{+0.038}_{-0.036}$	$0.061^{+0.055}_{-0.041}$	$18.056^{+0.018}_{-0.017}$	$0.052^{+0.026}_{-0.028}$	$18.029^{+0.022}_{-0.021}$	$0.142^{+0.023}_{-0.022}$
WD 1536+520	$17.749^{+0.011}_{-0.011}$	$0.011^{+0.012}_{-0.008}$	$17.546^{+0.011}_{-0.011}$	$0.019^{+0.016}_{-0.013}$	$16.830^{+0.009}_{-0.008}$	$0.042^{+0.010}_{-0.010}$
WD 1551+175	$17.642^{+0.015}_{-0.015}$	$0.028^{+0.021}_{-0.017}$	$17.736^{+0.014}_{-0.013}$	$0.031^{+0.019}_{-0.019}$	$17.708^{+0.018}_{-0.017}$	$0.086^{+0.021}_{-0.021}$
WD 1554+094	$19.019^{+0.033}_{-0.033}$	$0.039^{+0.042}_{-0.027}$	$18.973^{+0.045}_{-0.042}$	$0.193^{+0.047}_{-0.042}$	$18.662^{+0.035}_{-0.034}$	$0.194^{+0.037}_{-0.036}$
WD J1617+1620	$17.337^{+0.011}_{-0.011}$	$0.018^{+0.016}_{-0.012}$	$17.202^{+0.013}_{-0.013}$	$0.049^{+0.015}_{-0.013}$	$16.865^{+0.012}_{-0.012}$	$0.026^{+0.020}_{-0.017}$
WD 1729+371	$16.130^{+0.005}_{-0.005}$	$0.008^{+0.007}_{-0.005}$	$16.068^{+0.007}_{-0.007}$	$0.012^{+0.011}_{-0.008}$	$15.853^{+0.006}_{-0.006}$	$0.008^{+0.008}_{-0.005}$
WD 1929+011	$14.820^{+0.006}_{-0.006}$	$0.006^{+0.008}_{-0.004}$	$14.843^{+0.007}_{-0.007}$	$0.011^{+0.009}_{-0.007}$	$14.656^{+0.007}_{-0.007}$	$0.007^{+0.008}_{-0.005}$
WD 2132+096	$16.238^{+0.005}_{-0.005}$	$0.006^{+0.006}_{-0.004}$	$16.283^{+0.009}_{-0.009}$	$0.015^{+0.013}_{-0.010}$	$16.282^{+0.008}_{-0.008}$	$0.017^{+0.012}_{-0.011}$
WD 2207+121	$17.600^{+0.011}_{-0.011}$	$0.030^{+0.014}_{-0.013}$	$17.452^{+0.011}_{-0.010}$	$0.037^{+0.013}_{-0.014}$	$17.245^{+0.012}_{-0.011}$	$0.062^{+0.013}_{-0.013}$
WD 2221−165	$15.978^{+0.009}_{-0.010}$	$0.011^{+0.012}_{-0.008}$	$15.902^{+0.009}_{-0.009}$	$0.010^{+0.011}_{-0.007}$	$15.858^{+0.020}_{-0.021}$	$0.033^{+0.029}_{-0.022}$
WD 2326+049	$13.143^{+0.080}_{-0.078}$	$0.113^{+0.229}_{-0.058}$	$13.038^{+0.053}_{-0.049}$	$0.071^{+0.178}_{-0.037}$	$12.652^{+0.006}_{-0.006}$	$0.011^{+0.009}_{-0.007}$
WD 2328+107	$15.999^{+0.004}_{-0.004}$	$0.007^{+0.006}_{-0.005}$	$16.004^{+0.006}_{-0.006}$	$0.006^{+0.007}_{-0.004}$	$16.071^{+0.011}_{-0.011}$	$0.024^{+0.015}_{-0.015}$

dust emission. Consistent fluxes in the K band imply there was little change in the K band dust emission for the white dwarfs. A few objects stand out from the plots, these objects are discussed further in the following section. We also comment on some previously variable objects from the literature that were observed in this monitoring campaign.

3.3 Discussion of Individual Sources:

3.3.1 *WD 1145+017*

Vanderburg et al. (2015) discovered that WD 1145+017 is transited by multiple disintegrating planetesimals. The transit periods were approximately 4.5 hours and lasted various lengths from minutes to hours, with varying transit depths, the deepest of which blocks 60% of the flux from the star in the optical. The transits were not always present, and the transit activity level was variable (Gary et al. 2017).

The pink inverted triangle in Figs. 2a, 2b, and 2c show WD 1145+017 was variable at 4.1σ in the J band, 2.1σ in the H band, and was not significantly variable in the K band. From the UKIRT light curves of this white dwarf, shown in Fig. 3, it appears that the J band and possibly H
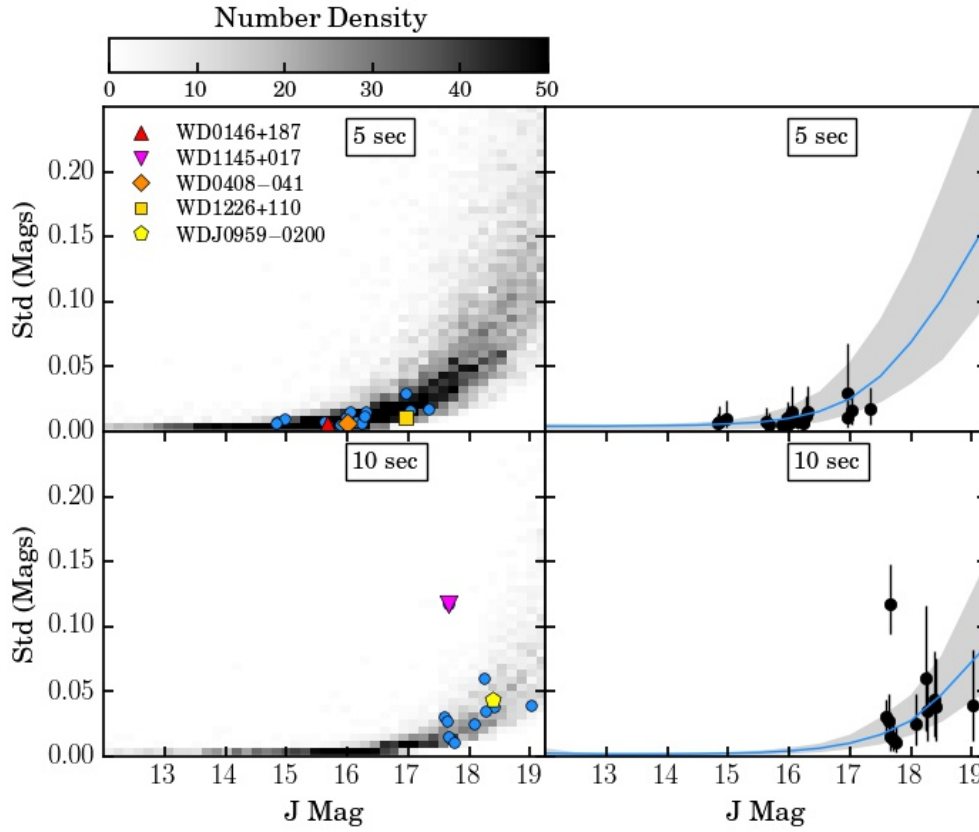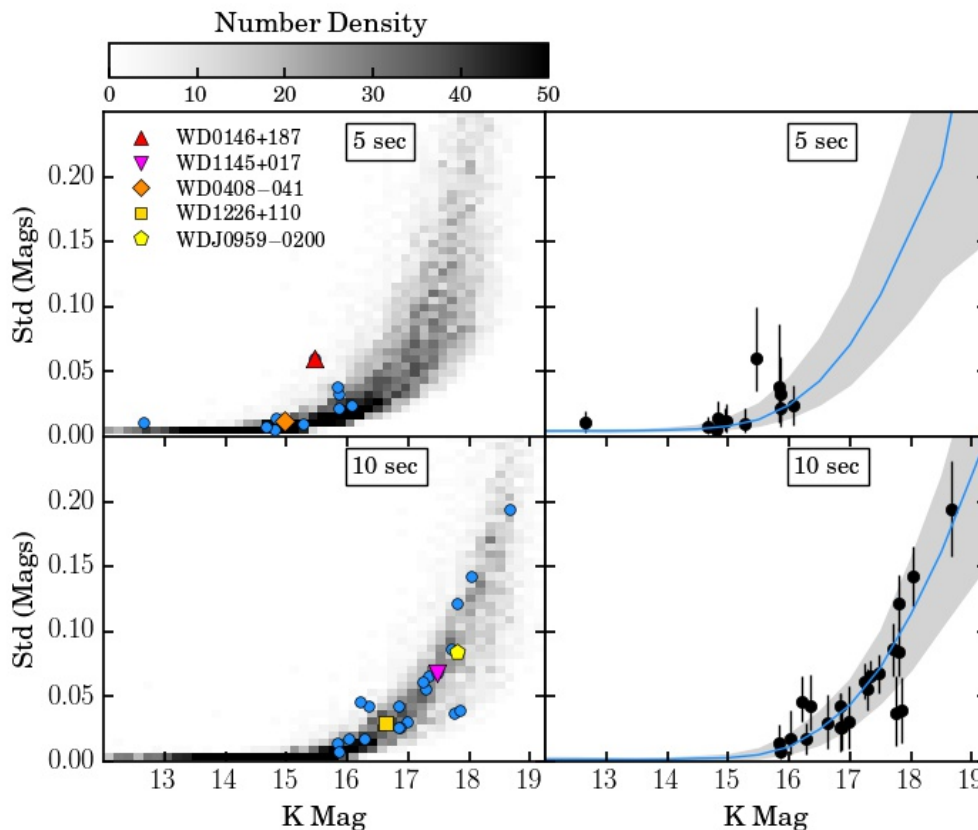
(a) *J* Band Observations
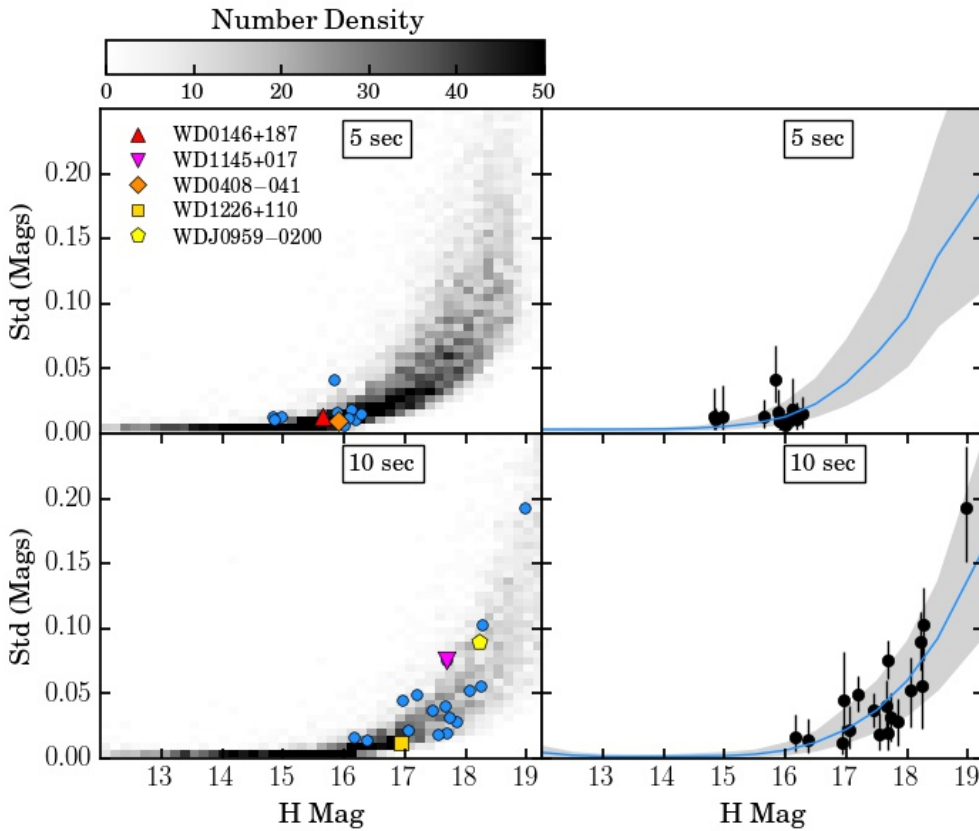
(b) *H* Band Observations

Figure 2.

(c) *K* Band Observations

Figure 2. The median observed magnitudes in the (a) *J*, (b) *H* and (c) *K* bands plotted against the median standard deviation of this magnitude for all white dwarfs and field stars. The two different observing modes, with 5 and 10 second frame times, are analysed separately. The density plots on the left hand side show the parameters for all field stellar objects in the field of view, there are of the order 10^4 field stars in each plot. The blue points show the white dwarfs, with the objects discussed in Section 3.3 labelled. The right hand plots show the median magnitude and standard deviation with the 16th and 84th percentile confidence levels for field stars in bins of width 0.5 mag. This forms a distribution about that median which should not comprise contaminant variable stars. The white dwarfs are plotted in black with the same values as in the left hand plots, but also including the 16th and 84th percentiles. This plot can be used to distinguish white dwarfs which are variable from those that follow the field star distribution.

band magnitudes were fainter on 09/05/2017. The *J*, *H* and *K* band observations were taken consecutively, the length of the observations were 3.5, 7.5 and 17 minutes respectively. Therefore, as the median dip duration is 9 minutes (Gary et al. 2017), it is possible that the transit occurred during the *J* band observations, with an overlap into the *H* band observations. Alternatively, as the variability was strongest in the *J* band and weakest in the *K* band it is consistent with the transit depth measurements found in Xu et al. (2018a), and could also explain the differences in the observed variability. Near contemporaneous optical observations indeed show transits in the light curve (B. Gary, private communications[2] Rappaport et al. 2017). The decrease in the *J* and *H* band flux is very likely to be caused by transits, rather than dust variability.

3.3.2 *WD 0146+187*

The object with the most significant deviation in the *K* band was WD 0146+187. In Fig. 2c the red triangle, which represents this object, shows a 2σ variability in the *K* band. There was a flux brightening of 0.14 mag from the 1st to the 2nd stacked frames on 03/10/14. There were no significant variations between the subsequent frames. Further investigations revealed there was nothing anomalous in the pixel map, and objects in the field of view within $100''$ do not show the same brightening trend. This could be a real change, but as there is only one data point, and the variation is not statistically significant, it is difficult to make any substantial conclusions.

3.3.3 *WD J0959−0200*

WD J0959−0200 was previously observed to display a 35% flux drop in 2010 in both *Spitzer* 3.6 and 4.5 μm Infrared Array Camera (IRAC) channels. The *K* band flux also dropped by 18.5% between 2005 and 2014 (Xu & Jura 2014). This variability measurement uses the peak-to-peak method,

---

[2] http://www.brucegary.net/zombie6/
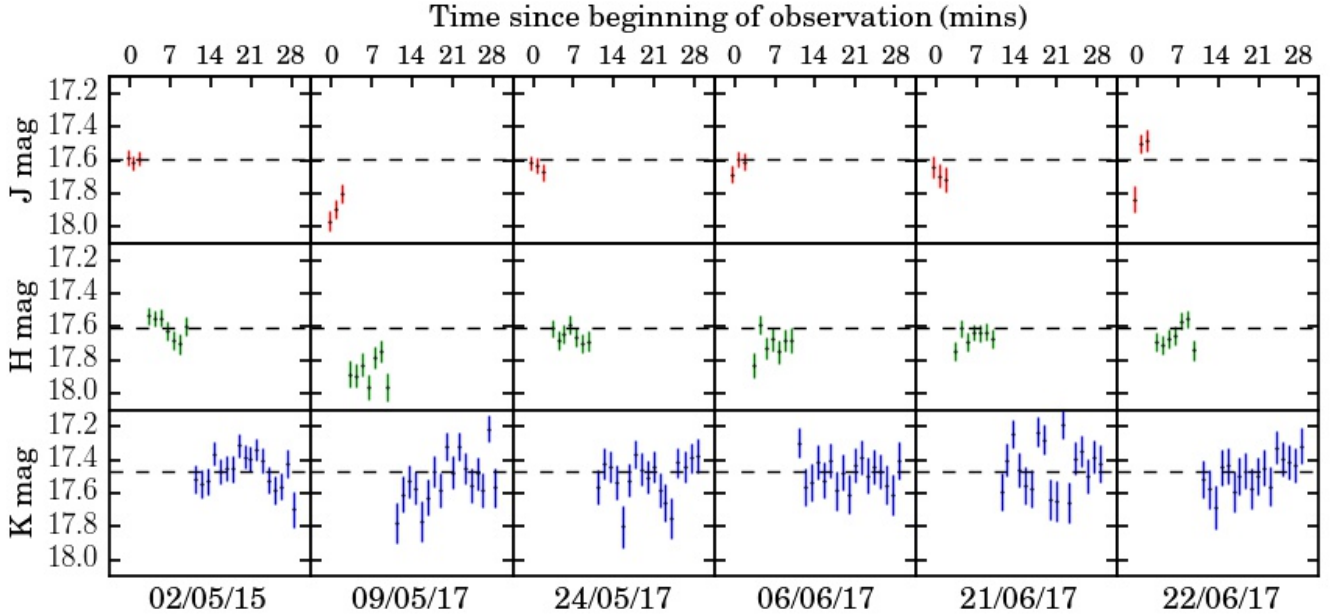
Figure 3. A light curve in the *J*, *H* and *K* bands for WD 1145+017. At each observation date a number of observations were taken in the *J*, *H* and *K* bands, totalling 28 minutes. The dotted lines show the mean magnitude for each band calculated from the first observation date, 02/05/15. This highlights how there was an apparent dip on 09/05/19 in the flux in the *J* and *H* bands attributed to dust transit features.

where the maximum flux change between two frames is quoted. After the Xu & Jura (2014) UKIRT data taken on the 27/03/14, in this work the *K* band data were consistent between multiple observations spanning 1153 days (Nov 2014, Feb 2015, Mar 2016, May 2016, May 2017). The *K* band flux was stable within $7.5^{+1.6}_{-1.6}\%$ ($\sigma = 0.085^{+0.019}_{-0.019}$) over these observations, seen in Fig. 2c as the yellow pentagon.

3.3.4 WD 1226+110

WD 1226+110 was found with a peak-to-peak drop in flux of 20% in the *Spitzer* 3.6 and 4.5 μm bands, and 13% in the *K* band, when comparing the 2007 UKIRT Infrared Deep Sky Survey *K* band flux with the 2015 UKIRT observation in this work (Xu et al. 2018b). Since 2015, this UKIRT survey has shown no significant changes in flux for WD 1226+110 between multiple observations separated by 738 days (May 2015, Feb 2016, May 2016, May 2017). The *K* band flux was stable within $2.7^{+1.9}_{-1.7}\%$ ($\sigma = 0.029^{+0.022}_{-0.019}$) for these observations, seen in Fig. 2c as the gold square.

3.3.5 WD 0408−041

WD 0408−041 (GD56) has previously been observed with dust emission variations at 3–5 μm showing brightening and dimming with peak-to-peak changes of 20% over 11.2 yrs (Farihi et al. 2018). This was attributed to dust production and consequentially depletion. In this work, the fluxes were found to be consistent between multiple observations separated by 851 days (Oct 2014, Oct 2016, Jan 2017). The *K* band dust emission appears to be stable within $1.1^{+1.2}_{-0.8}\%$ ($\sigma = 0.012^{+0.014}_{-0.008}$) for these observations, seen in Fig. 2c as

Table 3. The level of variability that can be detected at each magnitude in the *K* band, calculated from the field stars. The objects which were observed with 5 and 10 second frames were analysed separately. The median percentage variability is quoted for the field stars in bins with a width of one mag, along with the 16th and 84th percentiles.

Magnitude	5 s variability (%)	10 s variability (%)
11.0-12.0	$0.41^{+0.08}_{-0.02}$	$0.20^{+0.27}_{-0.08}$
12.0-13.0	$0.41^{+0.07}_{-0.02}$	$0.15^{+0.14}_{-0.04}$
13.0-14.0	$0.43^{+0.10}_{-0.04}$	$0.14^{+0.12}_{-0.04}$
14.0-15.0	$0.57^{+0.29}_{-0.11}$	$0.20^{+0.18}_{-0.07}$
15.0-16.0	$1.27^{+1.31}_{-0.51}$	$0.52^{+0.58}_{-0.27}$
16.0-17.0	$3.91^{+3.47}_{-1.75}$	$2.32^{+1.65}_{-1.17}$
17.0-18.0	$9.43^{+6.23}_{-3.89}$	$6.34^{+3.33}_{-2.52}$
18.0-19.0	$16.14^{+7.67}_{-6.48}$	$13.16^{+5.38}_{-4.62}$

the orange diamond. WD 0408−041 will be discussed again in Section 4.2 in reference to the *Spitzer* variability.

3.4 Expected Variability

We used the UKIRT survey to determine the level at which variability could be detected and ruled out. Table 3 shows the level of variability that can be detected at each *K* band magnitude. For each non-variable star in the fields of views of the white dwarfs, we have the median standard deviation of the magnitude measurements from the MCMC model. The level of variability is the median value of the non-variable
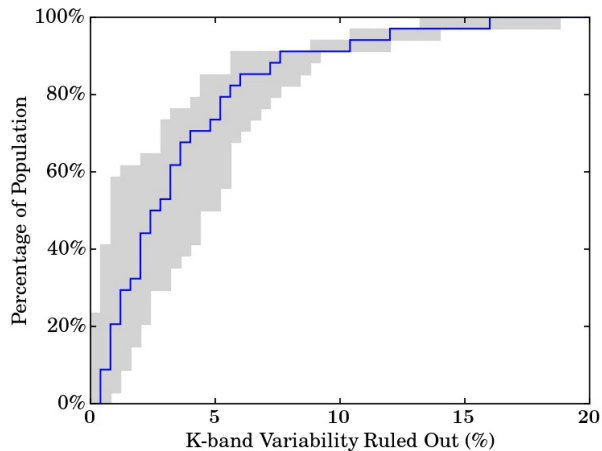
Figure 4. A cumulative distribution showing the level of K band variability that can be ruled out for the white dwarfs. The blue line shows the median cumulative distribution, with the contours as the cumulative distribution on the upper and lower limits (16th and 84th percentiles). For 90% of the sample, the K band flux varied by less than 10%.

stars' standard deviations, found in magnitude bins with a width of one mag. This median standard deviation was then converted to a percentage in flux space. We can rule out K band flux variability at $1.3^{+1.3}_{-0.5}$ % for objects brighter than 16th mag in the K band, and at $9.4^{+6.2}_{-3.4}$ % for objects brighter than 18th mag.

Fig. 4 shows a cumulative distribution of the level of variability we rule out for all white dwarfs. In other words, the percentage of white dwarfs where the K band flux was seen to vary by no more than the plotted value. This was calculated as the median standard deviation converted to a percentage in flux space. This was also calculated for the 16th and 84th percentile errors, which is shown as the shaded region in the figure. The K band flux of each white dwarf cannot have varied more than its equivalent standard deviation. Therefore, the K band flux has varied at less than 16.4 ± 2.8% for the entire sample, and less than $2.88^{+2.5}_{-1.9}$% for the median case. For greater than 90% of our sample we rule out variability at the 10% level, and for the 10 most constrained cases, we rule out variability at the percent level, $1.57^{+1.1}_{-1.0}$%.

Fig. 5a shows the percentage variability we rule out for each white dwarf plotted against the maximum time-scale over which that white dwarf was monitored in this survey. For example, for the white dwarf monitored over the longest period, WD 1929+011, we rule out variability at the $0.7^{+0.7}_{-0.5}$ % level over a time-scale of 1013 days.

There are a handful of objects in the literature with previous detections of a change in their dusty emission, as discussed in Section 3.3. For WD J0959−0200, Xu & Jura (2014) found a drop in K band flux from 57 μJy to 46 μJy which is equivalent to a peak-to-peak drop of 18.5%, and Xu et al. (2018b) found a K band peak-to-peak drop of 13% for WD 1226+110. We note the difficulty in comparing the peak-to-peak variability quoted for these objects with the median variability quoted in this work. With two measure-

ments it is not possible to constrain the distribution of fluxes that an object could be demonstrating, so the quoted variability is peak-to-peak. As we have more K band measurements, we use a median variability for all white dwarfs, and compare this to the distribution of the field objects to constrain the level of variability. Typically, peak-to-peak variability is larger than the medium variability that we adopted here. The peak-to-peak variability was also calculated for our sample using the maximum difference between the mean flux at each observation date, and the conclusions are consistent. In this sample we are able to rule out equivalent peak-to-peak variability and median variability for all white dwarfs during the time-scales observed. Our observations of both WD J0959−0200 and WD 1226+110 suggest that we are capable of detecting the same level of variability as observed previously, and yet we detect no such variability during our survey time span for all white dwarfs.

4 DISCUSSION

4.1 K Band Excess

For all objects in the sample, a white dwarf atmospheric model was fitted to find the expected contribution from the white dwarf photosphere to the K band flux. The white dwarf model atmospheres were kindly provided by P. Dufour using models from the Montreal white dwarf group (Bergeron et al. 2011; Coutu et al. 2019). The temperature, and log(g) used for the models are shown in Table 1; where possible, these parameters were taken from a previous photometric fit. For a number of white dwarfs where no photometric fit was available, we performed a new fit including data from the *Gaia* Data Release 2 (Prusti et al. 2016; Brown et al. 2018). The white dwarf radii (R) were determined from the photometric fit and the distances (D) were from the *Gaia* parallax (except for WD J0959−0200 which was from Farihi et al. (2012)). The SED fits are shown in Fig. B1 (available online); the photometric fit works well in most cases. Sometimes, additional adjustments were needed in R/D to improve the fits to the Sloan Digital Sky Survey (SDSS) and Pan-STARRS photometry. Those systems often had a large uncertainty in the parallax.

The white dwarf models were convolved with the bandpass of the UKIRT WFCAM K band filter (Hewett et al. 2006) to find the expected flux contribution from the white dwarf photosphere. From this, the excess flux associated with the dust was determined.

White dwarfs are usually photometrically stable and are often used as flux standards. A few white dwarfs in our sample are variable pulsators, however the optical variability is small, typically < 1%. Assuming the white dwarf photosphere displays no flux variations, we can convert the K band variability limit to the dust variability limit,

$$\sigma_{\text{dust}} = \sigma_{\text{K}} \frac{F_{\text{K}}}{F_{\text{K}} - F_{\text{WD}}}, \qquad (1)$$

where σ_{dust} is the variability constraint for the dust, σ_{K} is the variability constraint for the K band (dust and photosphere), F_{K} is the UKIRT K band flux measurement, and F_{WD} is the convolved model flux in the K band for the white dwarf photosphere. This puts a constraint on how much the

dust could have changed without being detected in this survey assuming the star remains constant.

We use the maximum variability not detected in the K band and convert it to a maximum variability not detected in the dusty emission using equation 1. Fig. 5b is a similar plot to Fig. 5a, but instead showing the level of variability we ruled out for the dusty emission. A K band excess is seen for 23/34 of the white dwarfs, as seen in the SEDs in Fig. B1 (available online). The 11 white dwarfs without a significant K band excess are: WD 0106−328, WD 0300−013, WD 0307+077, WD 1041+092, WD 1225−079, WD 1456+298, WD 2132+096, WD 2221−165, WD 2328+107, WD 1504+329, and WD 1551+175. For the 23 objects with significant K band excess, we put limits on how much dust variation could be hidden from detection. For 11 white dwarfs (∼ 50% of the sample with significant K band excesses) we constrained dust changes to be less than 10%, demonstrating the dust emission was stable over the course of the monitoring period. For the 11 systems where the K band excess is negligible, the dust variability constraint would have been 100%. For these objects we were only sensitive to an increase in dust emission, not a decrease. Therefore, the dust could have completely disappeared, and we could not distinguish this from the dust displaying no variability. For those with no significant K band excess, it is imperative to go to the mid-infrared for dust variability searches.

4.2 Expected Variability at 4.5 μm

Using the variability constraint derived from our UKIRT survey, we can predict the expected variability at 4.5 μm by assuming the dust emission has a constant colour temperature (i.e., the change is due to the amount of dust, not the location). So the shape of the dusty emission is assumed to remain constant, such that the percentage change of the dusty emission at K wavlengths can be equalled to the percentage change at 4.5 μm. Paralleling the K band analysis and equation 1, we can calculate the expected variability at *Spitzer* 4.5 μm wavelengths,

$$\sigma_{[4.5]} = \sigma_{\text{dust}} \frac{F_{[4.5]} - F_{\text{WD}}}{F_{[4.5]}}, \tag{2}$$

where $\sigma_{[4.5]}$ is the predicted variability constraint for the 4.5 μm *Spitzer* waveband, σ_{dust} is calculated from the K band using equation 1, $F_{[4.5]}$ is the 4.5 μm *Spitzer* flux, and F_{WD} is the convolved model flux in the 4.5 μm band for the white dwarf photosphere.

Fig. 6 shows the K band variability constraint, converted into a *Spitzer* 4.5 μm band variability constraint using equation 2. The *Spitzer* data was taken from the references listed in Table 1. If there was no *Spitzer* 4.5 μm data available then *WISE* 4.6 μm data was used instead. The dust excess at 4.5 μm is larger than that at the K band, therefore, the variability constraint in flux units will be larger for 4.5 μm, as seen in the figure. Those white dwarfs with negligible K band excess are excluded from this study. For those 23 white dwarfs with significant K band excess, at *Spitzer* wavelengths we predict that variability can be ruled out above 10% for ∼60% of our sample, above 20% for ∼ 85% of our sample, and above 36% for all our sample.

A particular application using our survey can be applied to WD 0408−041 system. Farihi et al. (2018) found the dust emission of WD 0408−041 to increase and decrease with a peak-to-peak variability of 20% over ∼ 11 years. As can be seen from Fig. B1 (available online), the SED of WD 0408−041 demonstrates a large K band excess. Therefore, any variability observed at mid-infrared wavelengths should be mimicked at a lower level in the K band, unless there is a colour change associated with the flux change. Fig. 7 shows the light curve for WD 0408−041 over approximately four years showing *Spitzer*, *WISE* and UKIRT K band data. The drop in mid-infrared flux is evident. We do not have UKIRT K band observations which cover the full mid-infrared time-scale, as shown by the blue shaded region. Using equations 1 and 2, the K band variability we ruled out using the UKIRT survey is scaled up to mid-infrared wavelengths. The change in the *Spitzer* 4.5 μm flux is consistent with the variability constraint derived from the K band data, implying that the variability could be consistent with the same colour temperature of the dust emission during the three year UKIRT survey. However, if we look across the four year baseline, even at 3 σ, the *Spitzer* flux values lie outside of the shaded region, i.e. prior to 56880 MJD and after 58100 MJD. The most significant drop in *Spitzer* flux was around 58100 days. We do not have simultaneous K band observations, with the closest K band measurement being over a year previous to this. There is previous evidence that large scale flux changes can occur on time-scales of less than a year (Xu & Jura 2014). A further K band measurement is needed in order to understand whether the K band flux also dropped around MJD58100, or if there is a colour change associated with this variability.

4.3 Variability Time-scales

Fig. 8 shows the characteristic sampling for all the white dwarfs in the sample. This survey was sensitive to short time-scales on the order of minutes to hours and long time-scales on the order of years. Previous examples of gas variability show changes on both these time-scales, and dust variability show changes on year long time-scales (e.g. Xu & Jura 2014; Manser et al. 2019).

We considered a toy model where the K band flux of every white dwarf varies as a step function by Δ%, every t days. We calculated the probability of detecting this variability in this UKIRT survey. Each white dwarf has a minimum detectable variability which is 3 σ above the median variability of the field stars at the same magnitude as the white dwarf, where σ is the standard deviation on this median variability. If Δ was smaller than the minimum detectable variability for that white dwarf, the probability of detection was 0. For every combination of Δ and t, the light curve was randomly sampled 1000 times for each white dwarf using the UKIRT sampling times to calculate the probability that if it were varying in this manner, it would have been detected in this survey. By averaging over all 34 white dwarfs at each Δ and t, the overall probability of detection was deduced, as shown in Fig. 9. The colour scheme represents the probability that the UKIRT survey would have detected that combination of Δ and t if all white dwarfs varied in this way. The highest probability time-scales show that our survey was sensitive to variability over days, and years. We can rule out models
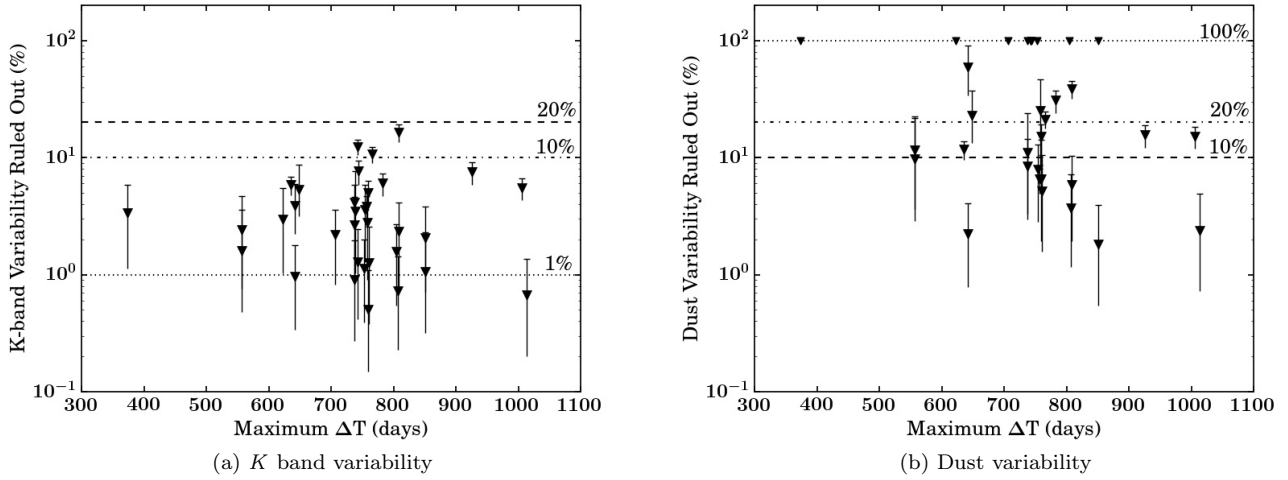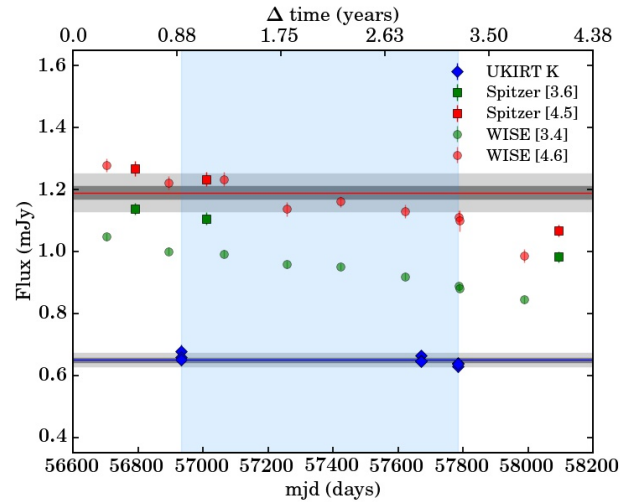
Figure 5. (a) The maximum *K* band median variability of each white dwarf that would not have been detected over the time-scale of the survey. (b) The maximum dust variability of each white dwarf that would not have been detected over the time-scale of the survey. The variability constraint of the dust component to the *K* band flux was calculated using equation 1.
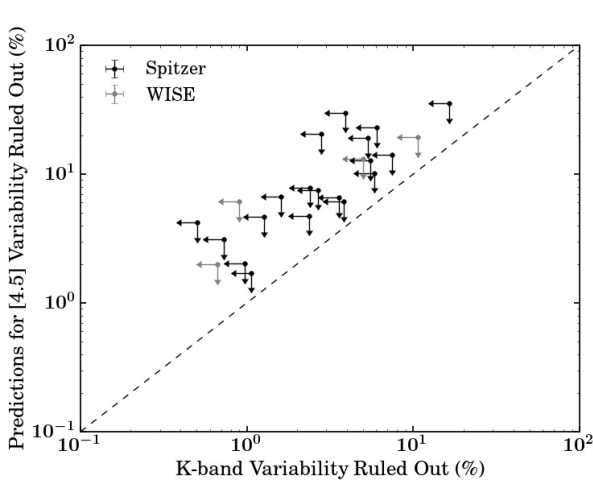
Figure 6. Predictions for the maximum median variability at $4.5\,\mu$m that would have escaped detection based on the maximum median *K* band variability not detected with this UKIRT survey. The arrows represent each axis is a constraint on the level of variability. Most objects had *Spitzer* $4.5\,\mu$m data, but for four objects *WISE* data was used as no *Spitzer* data was available.

Figure 7. A light curve of WD 0408−041 showing the UKIRT *K* band data, and the *Spitzer/WISE* data at which Farihi et al. (2018) observed a drop in the mid-infrared flux. The grey regions represent the 1 and $3\,\sigma$ median variability constraint for the *K* band, and then scaled up to *Spitzer* wavelengths using equations 1 and 2 (assuming a constant colour temperature). The blue region shows the period of time that we have UKIRT observations. Figure adapted from Farihi et al. (2018).

where all white dwarfs vary on time-scales of ~ 1–2 years with large amplitudes. However, we cannot rule out models where white dwarfs vary on time-scales much longer than this, or with smaller amplitudes ($< 10\%$). This may explain why some objects from the literature which have been previously found to vary, are consistent with little or no variability in this survey. For example, using seven years of *WISE* data, Swan et al. (2019) found variability in a number of dusty white dwarfs. Using this model we can see that for these longer time-scales, we have less than a 30% chance of detecting variability.

4.4 Implications

The leading explanation for white dwarf pollution cites asteroids as the source which are scattered inwards stochastically. How frequently these asteroids are scattered inwards remains an open question, with debate in the literature between whether pollution is caused by a single large body, or many small bodies (e.g. Jura 2008; Jura et al. 2009b; Wyatt et al. 2014).

Wyatt et al. (2014) presented a model whereby white dwarf pollution is explained by a continuous stream of many
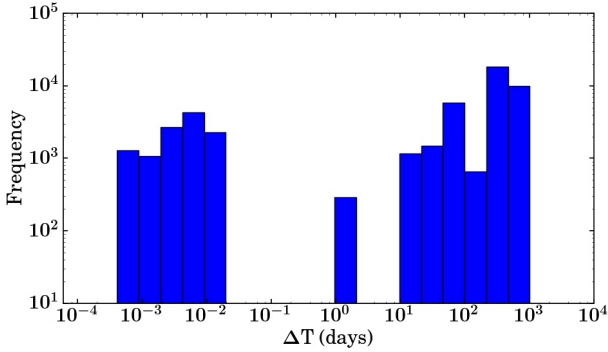
Figure 8. A histogram showing the characteristic survey sampling to search for variability. The plot shows the distribution of all time-scales between frames of a given white dwarf, for all white dwarfs. This demonstrates that for all white dwarfs our survey was sensitive to minute/hour time-scales and year time-scales.
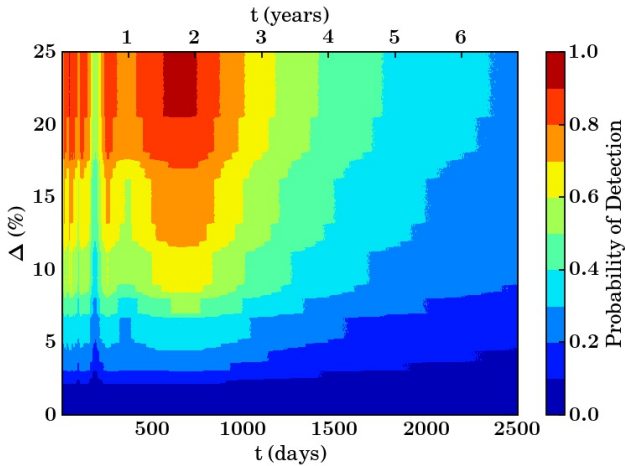
Figure 9. A toy model in which every white dwarf in our sample is considered to have a K band flux that varies by $\Delta\%$ every t days. The density plot indicates the probability of detecting that combination of Δ and t for white dwarfs in the UKIRT survey. The smallest grid scale is 1 day and 0.1%.

small asteroids, with the stochastic scattering of the largest bodies dominating the accretion rates. In this model, the lifetime of the dusty material is a free parameter, with a best-fitting value of 20 years. Our survey would be unlikely to detect variations on such long time-scales. However, if the disc lifetime was instead an order of magnitude smaller (~ 2 years), large amplitude variations in the infrared flux on these time-scales would be expected. In our survey, we rule out large variability over these time-scales. Therefore, the results of this survey provide further evidence in support of long (> 3 year) lifetimes for the dusty material around white dwarfs. It also demonstrates that disruption events large enough to be detectable in the infrared do not regularly occur on short time-scales such as years. This is crucial, as for many highly polluted DA white dwarfs, material can sink out of the atmospheres on time-scales of days to years. This

work provides observational evidence that dusty material has a lifetime of at least 2–3 years. Therefore, we highlight the need for further monitoring in the infrared to discover the frequency of scattering events.

5 CONCLUSIONS

Infrared studies are crucial for understanding the accretion processes associated with polluted white dwarfs. This work reports a near-infrared J, H, and K band monitoring campaign with the UKIRT, completed over three years which studied 34 polluted white dwarfs with infrared excesses. High precision J, H, and K band photometry was reported for the white dwarfs in the sample, for many of these objects high precision photometry is not previously reported. The main results are summarised as follows.

(i) The K band flux was stable within the error of the survey for all observations of the white dwarfs, where the observation sampling rates were on the order of minutes and years. Of the near-infrared bands, the K band is the most sensitive to the dust. We ruled out median K band variability greater than $16.4^{+2.8}_{-2.8}\%$ for the faintest white dwarf in the sample and less than $2.88^{+2.5}_{-1.9}\%$ for half of our sample. For $> 90\%$ of our sample we ruled out variability at the 10% level, and for our 10 most constrained white dwarfs we ruled out K band variability at the percent level, $< 1.57^{+1.1}_{-1.0}\%$.

(ii) WD J0959−0200 and WD 1226+110 have previously exhibited variability in their dusty emission as seen at the K band (18.5% for WD J0959−0200 and 13% for WD 1226+110) and *Spitzer* 3.6 and 4.5 μm bands. These objects did not display any significant variability in our study. For most of our sample (except our faintest object, WD 1554+094) we ruled out similar K band variability to these white dwarfs. This highlights that these large K band variability events are rare.

(iii) Assuming the dust emission does not change its colour temperature, we predicted variability at 4.5 μm based on the K band variability. We found that the white dwarfs should not vary at 4.5 μm above 10% for $\sim 60\%$ of our sample, above 20% for $\sim 85\%$ of our sample, and above 36% for all our sample.

(iv) We demonstrated that any white dwarf with large amplitude ($> 20\%$) near-infrared variability on short (< 3 year) time-scales should have been found with this survey. This implies that major tidal disruption events that lead to white dwarf pollution occur less frequently than every three years, and are consequently rare. Infrared variability around white dwarfs with infrared excesses does exist as revealed by other observations. The constraints provided from our K band survey imply that such events, if they occur, do so on short time-scales, and quickly become stable within a few years.

(v) Ground based near-infrared searches for white dwarf dust variability are fruitful, and as demonstrated in this survey can search for variability down to the percent level for the brightest sources. This survey was not sensitive to long time-scale (> 3 year) variability and, therefore, we highlight the need for long-term monitoring of white dwarfs with infrared excesses to fully understand these highly enigmatic and dynamic systems.

ACKNOWLEDGEMENTS

REFERENCES

Barber S. D., Kilic M., Brown W. R., Gianninas A., 2014, ApJ, 786, 77
Becklin E., Farihi J., Jura M., Song I., Weinberger A., Zuckerman B., 2005, ApJL, 632, L119
Bergeron P., Wesemael F., Dufour P., Beauchamp A., Hunter C., et al., 2011, ApJ, 737, 28
Bergfors C., Farihi J., Dufour P., Rocchetto M., 2014, MNRAS, 444, 2147
Bonsor A., Mustill A., Wyatt M. C., 2011, MNRAS, 414, 930
Brinkworth C., Gänsicke B. T., Marsh T., Hoard D. W., Tappert C., 2009, ApJ, 696, 1402
Brinkworth C., Gänsicke B., Girven J., Hoard D., Marsh T., Parsons S., Koester D., 2012, ApJ, 750, 86
Brown A., Vallenari A., Prusti T., De Bruijne J., Babusiaux C., Bailer-Jones C., Biermann M., et al., 2018, A & A, 616, A1
Coutu S., Dufour P., Bergeron P., Blouin S., Loranger E., Allard N., Dunlap B., 2019, ApJ, 885, 74
Debes J. H., Sigurdsson S., 2002, ApJ, 572, 556
Debes J. H., Hoard D., Wachter S., Leisawitz D. T., Cohen M., 2011, ApJS, 197, 38
Debes J. H., Walsh K. J., Stark C., 2012a, ApJ, 747, 148
Debes J., Kilic M., Faedi F., Shkolnik E., Lopez-Morales M., Weinberger A., Slesnick C., West R. G., 2012b, ApJ, 754, 59
Dennihy E., Clemens J., Dunlap B., Fanale S., Fuchs J., Hermes J., 2018, ApJ, 854, 40
Dufour P., Kilic M., Fontaine G., Bergeron P., Melis C., Bochanski J., 2012, ApJ, 749, 6
Dufour P., Blouin S., Coutu S., Fortin-Archambault M.,

Thibeault C., Bergeron P., Fontaine G., 2017, ASPC, 509, 3
Dye S., Warren S., Hambly N., Cross N., Hodgkin S., Irwin M., Lawrence A., et al., 2006, MNRAS, 372, 1227
Farihi J., Zuckerman B., Becklin E., 2008, ApJ, 674, 431
Farihi J., Jura M., Zuckerman B., 2009, ApJ, 694, 805
Farihi J., Barstow M., Redfield S., Dufour P., Hambly N., 2010a, MNRAS, 404, 2123
Farihi J., Jura M., Lee J.-E., Zuckerman B., 2010b, ApJ, 714, 1386
Farihi J., Brinkworth C., Gänsicke B., Marsh T., Girven J., Hoard D., Klein B., Koester D., 2011, ApJL, 728, L8
Farihi J., Gänsicke B., Steele P., Girven J., Burleigh M., Breedt E., Koester D., 2012, MNRAS, 421, 1635
Farihi J., Parsons S., Gänsicke B., 2017, Nature Astronomy, 1, 0032
Farihi J., van Lieshout R., Cauley P., Dennihy E., Su K., Kenyon S., et al., 2018, MNRAS, 481, 2601
Gänsicke B. T., Marsh T., Southworth J., Rebassa-Mansergas A., 2006, Science, 314, 1908
Gänsicke B., Marsh T., Southworth J., 2007, MNRAS:L, 380, L35
Gänsicke B., Koester D., Marsh T., Rebassa-Mansergas A., Southworth J., 2008, MNRAS:L, 391, L103
Gänsicke B. T., Schreiber M. R., Toloza O., Fusillo N. P. G., Koester D., Manser C. J., 2019, Nature, 576, 61
Gary B., Rappaport S., Kaye T., Alonso R., Hambsch F.-J., 2017, MNRAS, 465, 3267
Gelman A., Rubin D. B., et al., 1992, Statistical science, 7, 457
Gentile Fusillo N. P., Tremblay P.-E., Gänsicke B. T., Manser C. J., Cunningham T., Cukanovaite E., et al., 2018, MNRAS, 482, 4570
Girven J., Brinkworth C., Farihi J., Gänsicke B., Hoard D., Marsh T., Koester D., 2012, ApJ, 749, 154
Graham J. R., Matthews K., Neugebauer G., Soifer B., 1990, ApJ, 357, 216
Hamers A. S., Portegies Zwart S. F., 2016, MNRAS:L, 462, L84
Harrison J. H., Bonsor A., Madhusudhan N., 2018, MNRAS, 479, 3814
Hewett P. C., Warren S. J., Leggett S. K., Hodgkin S. T., 2006, MNRAS, 367, 454
Hollands M., Gänsicke B., Koester D., 2018, MNRAS, 477, 93
Irwin M. J., et al., 2004, in Optimizing scientific return for astronomy through information technologies. pp 411–422
Irwin J., Irwin M., Aigrain S., Hodgkin S., Hebb L., Moraux E., 2007, MNRAS, 375, 1449
Jura M., 2003, ApJL, 584, L91
Jura M., 2008, AJ, 135, 1785
Jura M., Young E., 2014, AREPS, 42, 45
Jura M., Farihi J., Zuckerman B., Becklin E., 2007a, AJ, 133, 1927
Jura M., Farihi J., Zuckerman B., 2007b, ApJ, 663, 1285
Jura M., Farihi J., Zuckerman B., 2009a, AJ, 137, 3191
Jura M., Muno M., Farihi J., Zuckerman B., 2009b, ApJ, 699, 1473
Jura M., Xu S., Klein B., Koester D., Zuckerman B., 2012, ApJ, 750, 69
Kilic M., von Hippel T., Leggett S., Winget D., 2006, ApJ, 646, 474
Klein B., Jura M., Koester D., Zuckerman B., 2011, ApJ, 741, 64
Koester D., 2009, A&A, 498, 517
Koester D., Napiwotzki R., Voss B., Homeier D., Reimers D., 2005, A & A, 439, 317
Koester D., Gaensicke B. T., Farihi J., 2014, A&A, 566, A34
Manser C. J., Gänsicke B. T., Marsh T. R., Veras D., Koester D., Breedt E., et al., 2015, MNRAS, 455, 4467
Manser C. J., Gänsicke B. T., Koester D., Marsh T. R., Southworth J., 2016, MNRAS, 462, 1461

Manser C. J., Gänsicke B. T., Eggl S., Hollands M., Izquierdo P., Koester D., et al., 2019, Science, 364, 66

Melis C., Dufour P., 2016, ApJ, 834, 1

Melis C., Jura M., Albert L., Klein B., Zuckerman B., 2010, ApJ, 722, 1078

Melis C., Dufour P., Farihi J., Bochanski J., Burgasser A. J., Parsons S., Gänsicke B., et al., 2012, ApJL, 751, L4

Mustill A. J., Villaver E., Veras D., Gänsicke B. T., Bonsor A., 2018, MNRAS, 476, 3939

Patil A., Huard D., Fonnesbeck C. J., 2010, Journal of statistical software, 35, 1

Payne M. J., Veras D., Holman M. J., Gänsicke B. T., 2016, MNRAS, 457, 217

Petrovich C., Muñoz D. J., 2017, ApJ, 834, 116

Prusti T., De Bruijne J., Brown A. G., Vallenari A., Babusiaux C., Bailer-Jones C., et al., 2016, A & A, 595, A1

Rappaport S., Gary B., Kaye T., Vanderburg A., Croll B., Benni P., Foote J., 2016, MNRAS, 458, 3904

Rappaport S., Gary B., Vanderburg A., Xu S., Pooley D., Mukai K., 2017, MNRAS, 474, 933

Reach W. T., Kuchner M. J., von Hippel T., Burrows A., Mullally F., Kilic M., Winget D., 2005, ApJL, 635, L161

Rebassa-Mansergas A., Solano E., Xu S., Rodrigo C., Jiménez-Esteban F., Torres S., 2019, MNRAS, 489, 3990

Rocchetto M., Farihi J., Gänsicke B., Bergfors C., 2015, MNRAS, 449, 574

Smallwood J. L., Martin R. G., Livio M., Lubow S. H., 2018, MNRAS, 480, 57

Stephan A. P., Naoz S., Zuckerman B., 2017, ApJL, 844, L16

Swan A., Farihi J., Wilson T. G., 2019, MNRAS:L, 484, L109

Vanderbosch Z., et al., 2019, arXiv preprint arXiv:1908.09839

Vanderburg A., Johnson J. A., Rappaport S., Bieryla A., Irwin J., et al., 2015, Nature, 526, 546

Veras D., Wyatt M. C., Mustill A. J., Bonsor A., Eldridge J. J., 2011, MNRAS, 417, 2104

Veras D., Leinhardt Z. M., Bonsor A., Gänsicke B. T., 2014, MNRAS, 445, 2244

Veras D., Georgakarakos N., Dobbs-Dixon I., Gänsicke B. T., 2016, MNRAS, 465, 2053

Voss B., Koester D., Napiwotzki R., Christlieb N., Reimers D., 2007, A & A, 470, 1079

Wang T.-g., Jiang N., Ge J., Cutri R. M., Jiang P., Sheng Z., et al., 2019, ApJL, 886, L5

Wilson D. J., Gänsicke B. T., Koester D., Raddi R., Breedt E., Southworth J., Parsons S. G., 2014, MNRAS, 445, 1878

Wilson D. J., Gänsicke B. T., Koester D., Toloza O., Pala A. F., Breedt E., Parsons S. G., 2015, MNRAS, 451, 3237

Wilson T. G., Farihi J., Gänsicke B. T., Swan A., 2019, MNRAS, 487, 133

Wyatt M., Farihi J., Pringle J., Bonsor A., 2014, MNRAS, 439, 3371

Xu S., Jura M., 2012, ApJ, 745, 88

Xu S., Jura M., 2014, ApJL, 792, L39

Xu S., Jura M., Klein B., Koester D., Zuckerman B., 2013, ApJ, 766, 132

Xu S., Jura M., Pantoja B., Klein B., Zuckerman B., Su K., Meng H., 2015, ApJL, 806, L5

Xu S., Zuckerman B., Dufour P., Young E., Klein B., Jura M., 2017, ApJL, 836, L7

Xu S., Rappaport S., van Lieshout R., Vanderburg A., Gary B., Hallakoun N., Ivanov V., et al., 2018a, MNRAS, 474, 4795

Xu S., Su K., Rogers L., Bonsor A., et al., 2018b, ApJ, 866, 108

Zuckerman B., Becklin E., 1987, Nature, 330, 138

Zuckerman B., Koester D., Reid I. N., Hünsch M., 2003, ApJ, 596, 477

Zuckerman B., Koester D., Melis C., Hansen B. M., Jura M., 2007, ApJ, 671, 872

Zuckerman B., Melis C., Klein B., Koester D., Jura M., 2010, ApJ, 722, 725

APPENDIX A: OBSERVATION INFORMATION

Table A1 shows the dates of the observations for each white dwarf in the sample. Table A2 shows the frame numbers for each white dwarf in the sample.

This paper has been typeset from a TeX/LaTeX file prepared by the author.

Table A1. All the polluted white dwarfs with an infrared excess observed with the UKIRT and the dates they were observed.

WD Name	2014B	2015A	2015B	2016A	2016A	2016B	2016B	2017A	2017A
WD 0010+280	03/10/14	N	N	N	N	06/07/16	N	N	N
WD 0106−328	03/10/14	N	N	N	N	11/10/16	N	N	N
WD 0146+187	03/10/14	N	N	N	N	12/07/16	N	N	N
WD 0300−013	03/10/14	N	N	N	N	22/07/16	31/01/17	N	N
WD 0307+077	03/10/14	N	N	N	N	10/10/16	N	N	
WD 0408−041	03/10/14	N	N	N	N	10/10/16	31/01/17	N	N
WD 0435+410	03/10/14	N	31/01/16	N	N	10/10/16	N	N	N
WD J0738+1835	N	03/05/15	N	29/02/16	N	10/10/16	28/01/17	N	N
WD J0959−0200	09/11/14	02/02/15	N	05/03/16	07/05/16	N	N	23/05/17	N
WD 1015+161	30/10/14	N	N	09/05/16	N	N	N	N	N
WD 1018+410	30/10/14	N	N	09/05/16	N	N	N	N	N
WD 1041+092	N	02/05/15	N	04/03/16	09/05/16	N	N	N	N
WD 1116+026	N	02/05/15	N	05/03/16	10/05/16	N	N	30/05/17	N
WD 1145+017	N	02/05/15	N	N	N	N	N	09/05/17	24/05/17*
WD 1145+288	N	02/05/15	N	23/02/16	09/05/16	N	N	30/05/17	N
WD 1150−153	N	03/05/15	N	05/03/16	10/05/16	N	N	01/06/17	N
WD J1221+1245	N	02/05/15	N	01/03/16	10/05/16	N	N	25/05/17	N
WD 1225−079	N	03/05/15	N	04/03/16	10/05/16	N	N	25/05/17	N
WD 1226+110	N	02/05/15	N	29/02/16	10/05/16	N	N	09/05/17	N
WD J1234+5606	N	03/05/15	N	04/03/16	05/06/16	N	N	07/06/17	N
WD 1349−230	N	03/05/15	N	04/03/16	06/06/16	N	N	30/05/17	N
WD 1456+298	N	02/05/15	N	17/02/16	10/05/16	N	N	14/05/17	N
WD 1504+329	N	01/05/15	N	29/02/16	08/05/16	N	N	12/05/17	N
WD 1536+520	N	02/05/15	N	05/03/16	29/05/16	N	N	28/05/17	N
WD 1551+175	N	01/05/15	N	03/03/16	31/05/16	N	N	14/05/17	N
WD 1554+094	N	01/05/15	N	29/02/16	08/05/16	N	N	20/05/17	18/07/17
WD J1617+1620	N	01/05/15	N	17/02/16	10/05/16	N	N	10/05/17	17/07/17
WD 1729+371	N	02/05/15	02/08/15	28/02/16	10/05/16	N	N	12/05/17	17/07/17
WD 1929+011	06/10/14	N	02/08/15	N	N	10/07/16	10/05/17	15/07/17	N
WD 2132+096	N	03/05/15	09/08/15	21/04/16	N	10/07/16	N	11/05/17	15/07/17
WD 2207+121	13/10/14	N	08/08/15	N	N	29/06/16	N	15/07/17	N
WD 2221−165	30/10/14	N	09/08/15	N	N	13/07/16	N	N	N
WD 2326+049	03/10/14	N	09/08/15	N	N	06/07/16	N	N	N
WD 2328+107	N	N	08/08/15	01/06/16	N	06/07/16	N	02/06/17	15/07/17

(*) For WD 1145+017, there are three more dates for 2017A: 06/06/2017, 21/06/2017 and 22/06/2017.

Table A2. All the polluted white dwarfs with an infrared excess observed with the UKIRT survey and the total number of frames. Each frame consists of a dithered stack of 5 exposures, each with the corresponding frame time of 5 or 10 seconds. FT = frame time for each individual exposure in the dithered stack, FN = total number of dithered stacks over all observations.

WD Name	FT J (secs)	FN J	FT H (secs)	FN H	FT K (secs)	FN K
WD 0010+280	5	6	10	6	10	10
WD 0106−328	5	6	5	6	5	6
WD 0146+187	5	6	5	6	5	6
WD 0300−013	5	6	5	6	5	9
WD 0307+077	5	6	10	6	10	10
WD 0408−041	5	9	5	9	5	9
WD 0435+410	5	3	5	3	5	9
WD J0738+1835	10	9	10	27	10	75
WD J0959−0200	10	9	10	27	10	75
WD 1015+161	5	6	5	6	10	6
WD 1018+410	5	6	10	6	10	10
WD 1041+092	10	9	10	21	10	51
WD 1116+026	5	4	5	4	5	12
WD 1145+017	10	18	10	42	10	102
WD 1145+288	10	12	10	28	10	68
WD 1150−153	5	12	5	11	10	12
WD J1221+1245	10	12	10	36	10	100
WD 1225−079	5	4	5	4	5	12
WD 1226+110	5	12	10	12	10	20
WD J1234+5606	10	9	10	27	10	75
WD 1349−230	5	12	10	12	10	20
WD 1456+298	5	3	5	3	5	6
WD 1504+329	10	9	10	27	10	75
WD 1536+520	10	12	10	28	10	68
WD 1551+175	10	12	10	28	10	68
WD 1554+094	10	15	10	45	10	125
WD J1617+1620	5	19	10	23	10	45
WD 1729+371	5	19	5	19	10	23
WD 1929+011	5	6	5	10	5	20
WD 2132+096	5	20	5	22	10	26
WD 2207+121	10	18	10	36	10	76
WD 2221−165	5	6	5	6	5	6
WD 2326+049	5	3	5	3	5	9
WD 2328+107	5	19	5	19	5	23
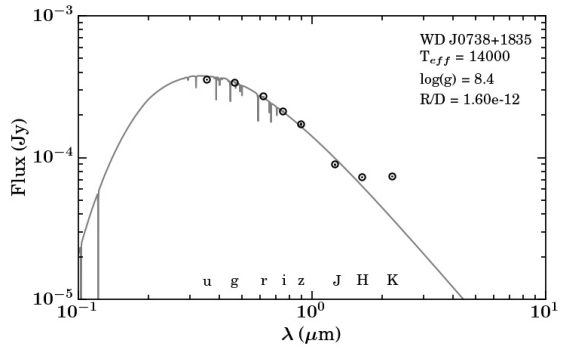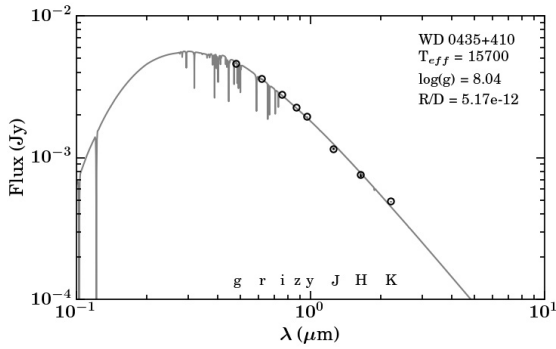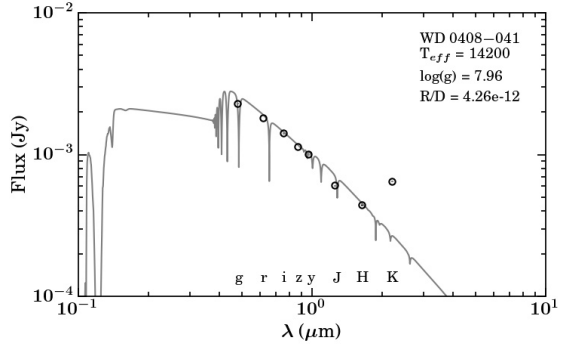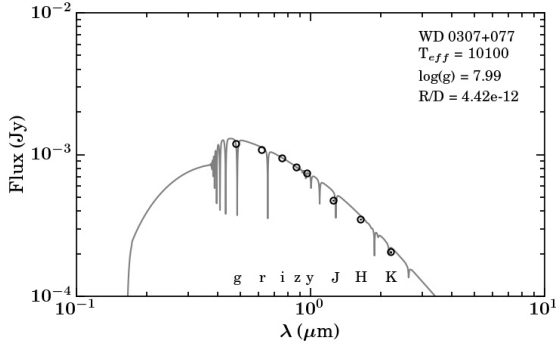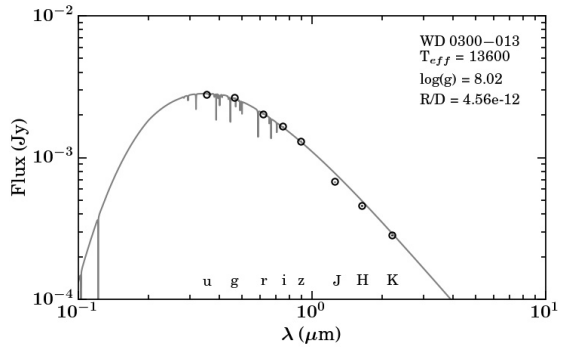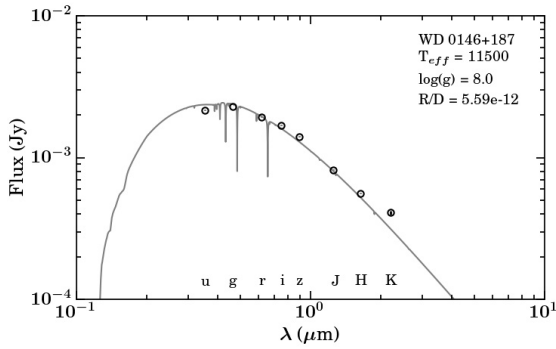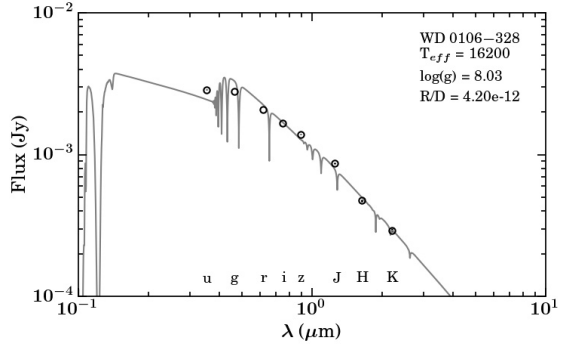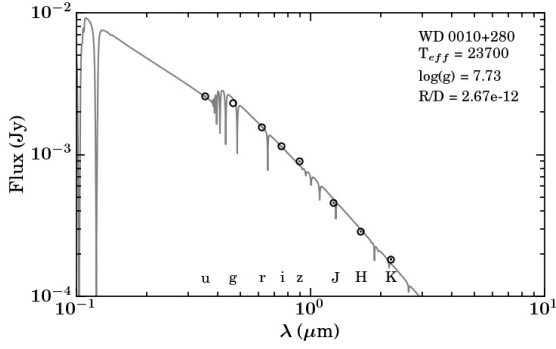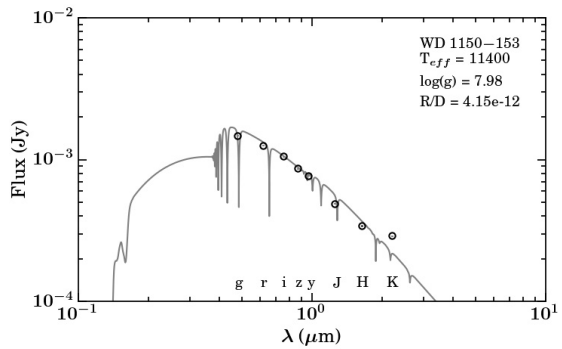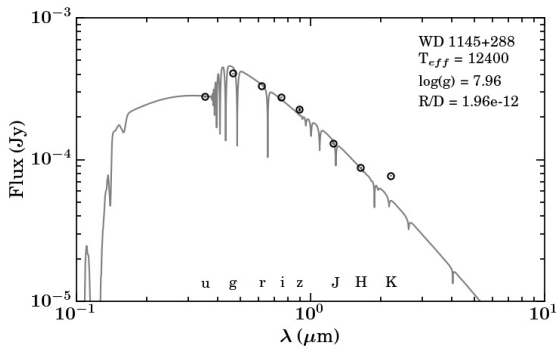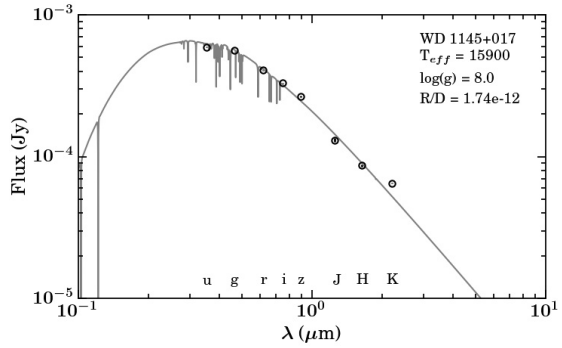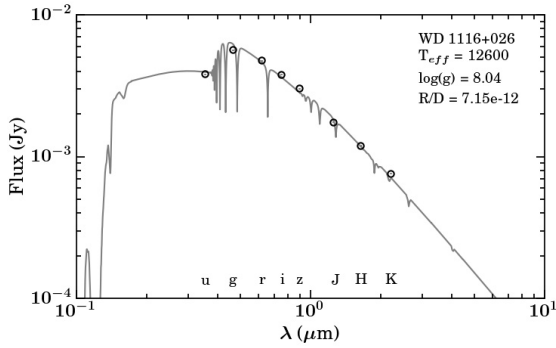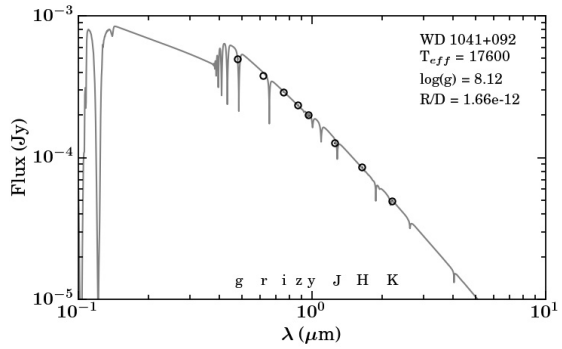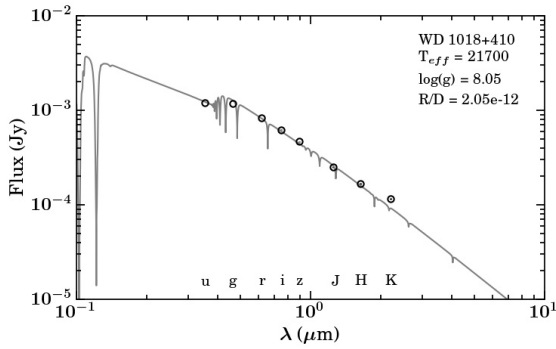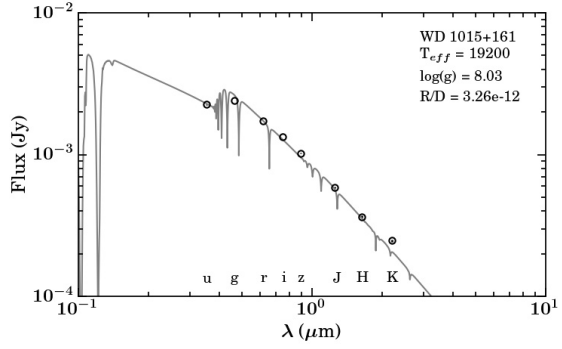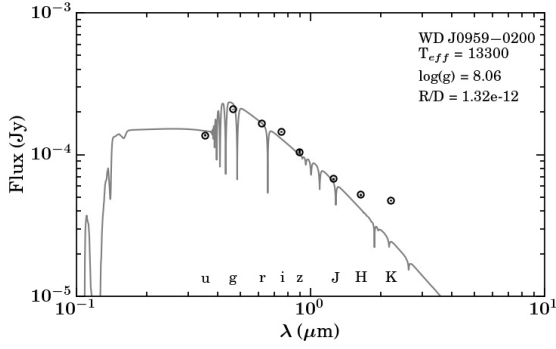
Figure B1.
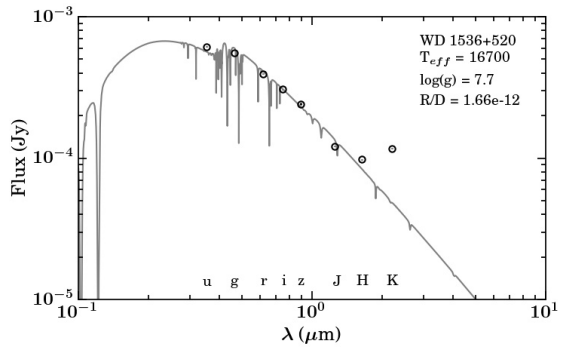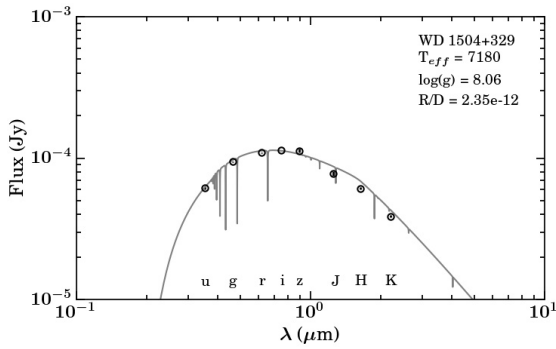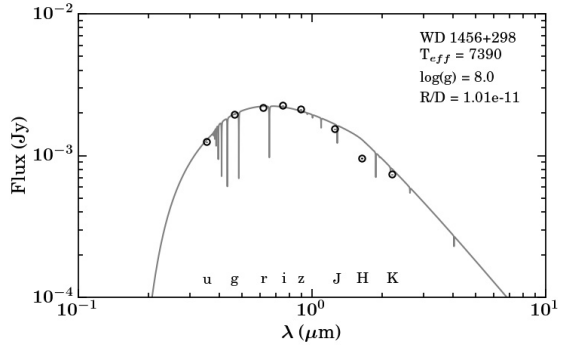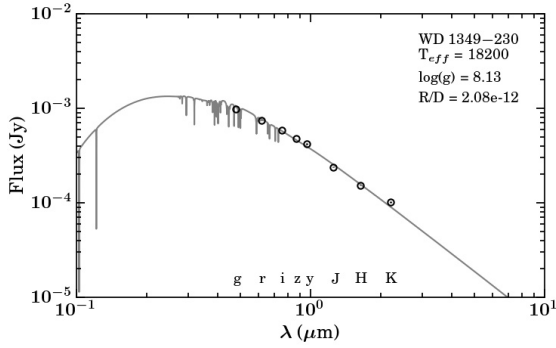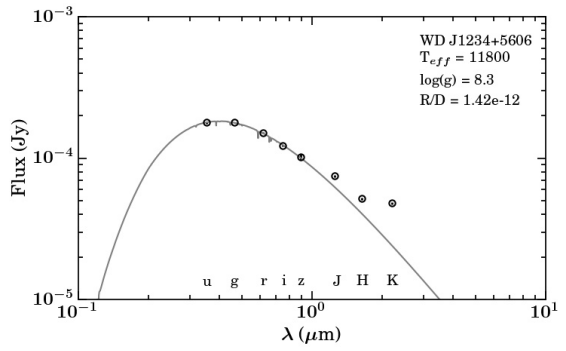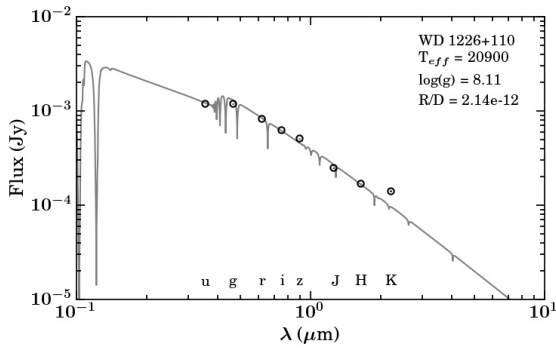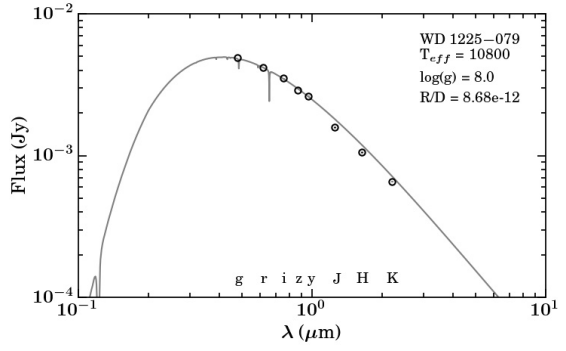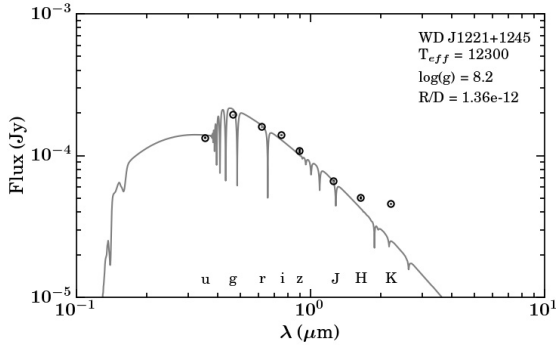
Figure B1.

Figure B1.

WD 1551+175
$T_{eff} = 15600$
$\log(g) = 7.96$
$R/D = 1.72e\text{-}12$

WD 1554+094
$T_{eff} = 21800$
$\log(g) = 7.63$
$R/D = 7.53e\text{-}13$

WD J1617+1620
$T_{eff} = 13200$
$\log(g) = 8.04$
$R/D = 2.20e\text{-}12$

WD 1729+371
$T_{eff} = 10300$
$\log(g) = 8.13$
$R/D = 4.99e\text{-}12$

WD 1929+011
$T_{eff} = 25400$
$\log(g) = 8.17$
$R/D = 4.90e\text{-}12$

WD 2132+096
$T_{eff} = 13100$
$\log(g) = 7.96$
$R/D = 3.80e\text{-}12$

WD 2207+121
$T_{eff} = 14800$
$\log(g) = 7.97$
$R/D = 1.81e\text{-}12$

WD 2221−165
$T_{eff} = 9900$
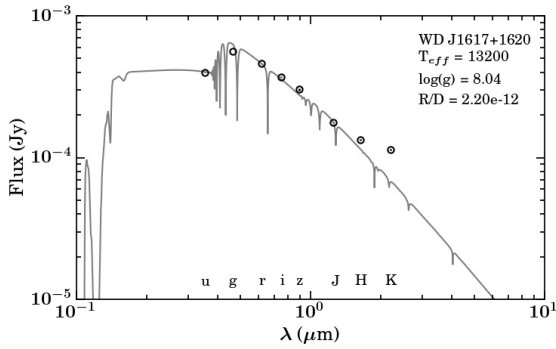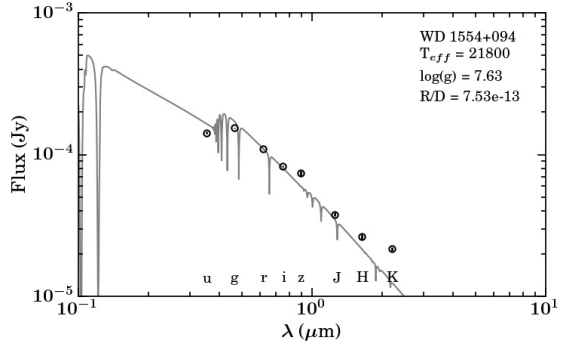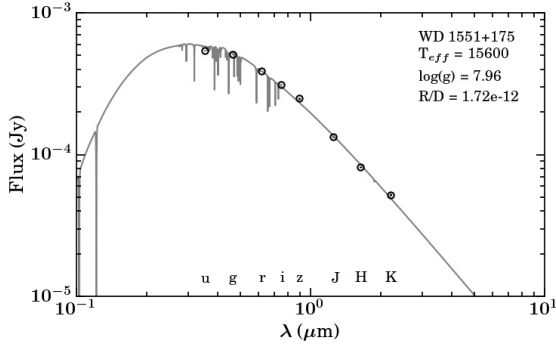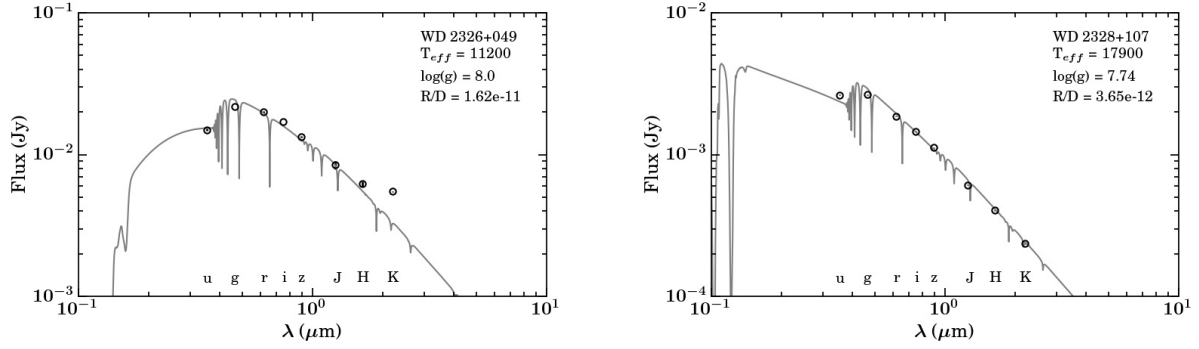$\log(g) = 8.12$
$R/D = 5.01e\text{-}12$
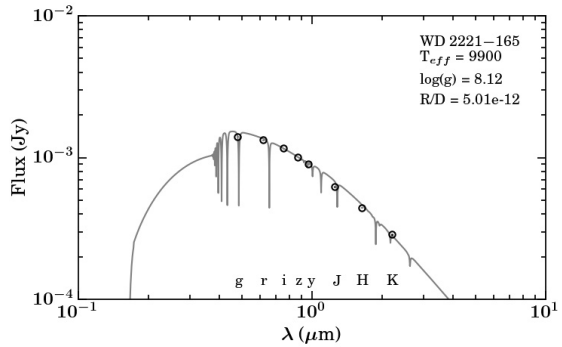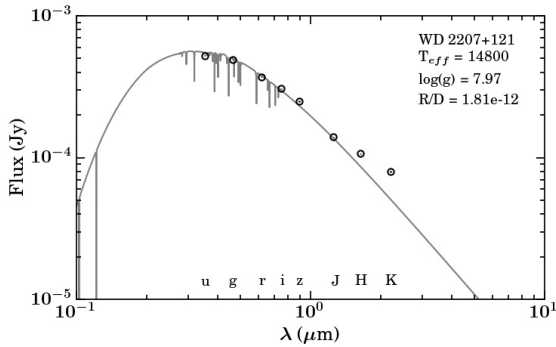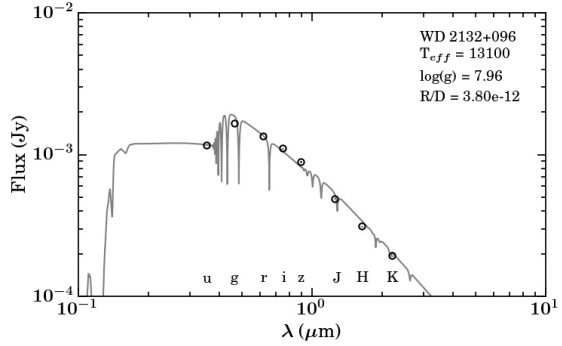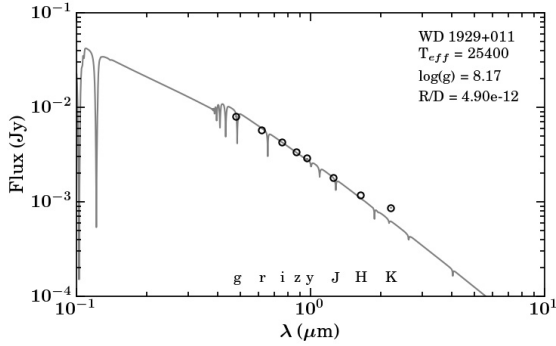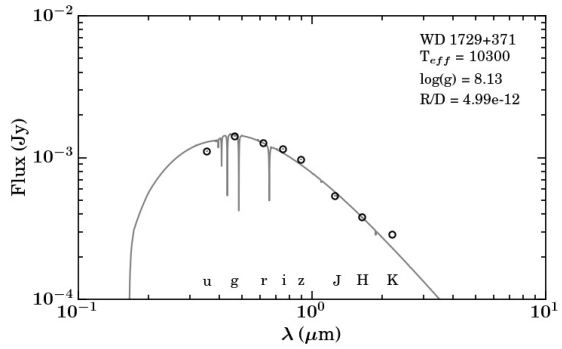
Figure B1.

Figure B1. The spectral energy distributions for the 34 white dwarfs in this sample. The temperature and log(g) used within the models are shown. R/D is the scaling factor used for the radii/distance needed in order for the models to fit the SDSS or Pan-STARRS optical data. The 11 white dwarfs without a significant K band excess are: WD 0106−328, WD 0300−013, WD 0307+077, WD 1041+092, WD 1225−079, WD 1456+298, WD 2132+096, WD 2221−165, WD 2328+107, WD 1504+329, and WD 1551+175.